Universität Zürich[UZH]

Empa
Materials Science and Technology

Alloying CdTe with Se, a possible route to improve CdTe solar cells

Annina Spescha

Master Thesis
16.06.2016

Accomplished in the Laboratory for Thin Films and Photovoltaics at Empa Dübendorf

Supervisors: M. Lingg, Dr. J. Perrenoud and Dr. S. Bücheler

Advisors: Prof. H. W. Fink and Dr. C. Escher

Abstract

Due to the possibility of fast and cost effective production CdTe is one of the most promising material for thin film solar cells. In the thin film photovoltaic technologies it has with over 10 % the highest market share mainly because of the company First Solar Inc.
The performance of conventional CdTe solar cells is mainly limited by the dopability and the recombination rate at the junction and the interface to the back contact.
Alloying CdTe with CdSe is a possible approach to enhance the solubility of the doping material by reducing the defect formation energy and to introduce preferable electric fields resulting in enhanced drift for the charge carriers to reduce recombination.
In this work first the influence of Selenium in a co-evaporated $CdTe_{1-x}Se_x$ alloy with x between 0 and 0.5 is analyzed. Depending on the composition the band gap can be tuned between 1.40 $\pm$ 0.02 eV and 1.48 $\pm$ 0.02 eV. The free charge carrier concentration of the Cu dopant was reduced and the resistivity of the absorber enhanced.
Second the influence of Selenium at the interface to the back contact and at the p-n junction is analyzed. Incorporation of a low amount of Selenium at the junction enhances the J_{SC} but the V_{OC} decreases. Selenium at the interface to the back contact enhances the J_{SC} but reduces V_{OC}. Another goal of the incorporation of CdSe at the junction is the reduction of the thickness of the CdS layer, which enhances the J_{SC} at low amounts of Selenium but the V_{OC} also decreases.
As a third concept the undoped $CdTe_{1-x}Se_x$ alloy is used as the intrinsic layer to investigate a p-i-n junction solar cell with CdS as the n-type layer and Spiro-OMeTAD and PTAA as the p-type layer. Alloys with x = 0.15, x = 0.20 and x = 0.25 were investigated, with absorber thicknesses of 500 nm and 1 µm where the thicker absorber with lower amount of Selenium results in a better cell performance. Spiro-OMeTAD gives a high V_{OC} but the J_{SC} of the samples with PTAA is much higher and in the range of the conventional CdTe cell (about 20 mA). The fill factor is also higher for the cells with the PTAA p-layer. The highest achieved efficiency with 1 µm absorber thickness and PTAA as a p-type layer was 10.1 % with a J_{SC} of 18.7 mA, a V_{OC} of 730 mV and a fill factor of 74 %.

Acknowledgment

I would like to thank Dr. Stephan Bücheler for giving me the opportunity to do my master thesis in this group and for giving important inputs and new ideas. I also like to thank Martina Lingg for the support during my time in the laboratory. Furthermore I'd like to thank Dr. Julian Perrenoud for helping even after leaving EMPA. A big thank goes to Fan Fu and Stefano Pisoni who made the spin coating for me and to all the other group members who always took their time to explain and help. At last I'd like to thank Prof. H.W. Fink and Dr. Conrad Escher for the support that made it possible to write my thesis at Empa.

Contents

1

Introduction

The leader in the solar cell market are still the silicon wafer-based modules, but thin film solar cells also play an important role. They need a lower amount of material. This allows a cheaper production which is faster and needs less energy. Among thin film PV technologies, CdTe solar cells have the highest market share.
The research of CdTe solar cells started already in the late 1950's in the USA. CdTe is a II-VI semiconductor with a direct band gap of 1.49 eV at room temperature and an absorption coefficient over 10^4 cm^{-1}. This material is very interesting because it is cost effective and its chemical and thermal stability allows a high production throughput. This leads to a short energy payback time of about 8 months. It is the most cost effective technology by now. The theoretical efficiency which can be achieved with a CdTe solar cell is about 30 % [16].
CdTe solar cells are mainly produced in the superstrate configuration (see Fig. 1.1 a). Empa is working on the substrate configuration (Fig. 1.1 right) which allows the use of substrates which are not transparent and therefore also flexible metal foils or other materials such as plastic can be used [6]. Another advantage of the substrate configuration is a better control of the junction formation [7]. The two different configurations are shown in Fig. 1.1.

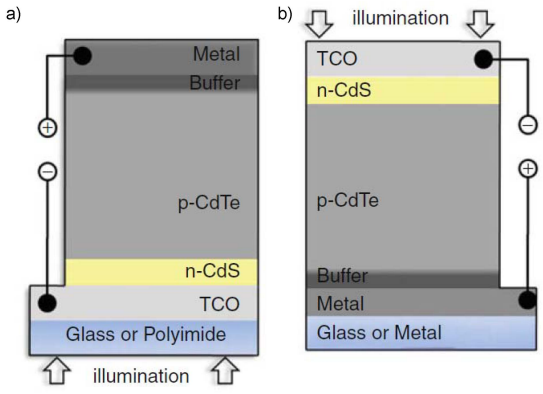

Figure 1.1: *The two possible configurations of CdTe solar cells are shown. In (a) the superstrate configuration is shown. The light has to penetrate the substrate which limits the choice of substrate materials. In (b) the substrate configuration is shown. This configuration allows, beside the wider range of possible substrates, a better junction and interface control during the fabrication.*

One of the main problems of CdTe is the dopability with Cu. The Cu atoms tend to segregate at the grain boundaries and the solubility in the bulk is limited [21]. The highest hole density that could be measured at Empa in 2013 was in the order of 10^{14} cm^{-3} for Cu doped CdTe solar cells [12]. What has been done so far to enhance the Cu concentration in the bulk is a short annealing and quenching (explained in Section 3.2.1). Due to this short annealing Cu atoms will diffuse from the grain boundaries into the bulk and the fast cool down allows to stop them rapidly in the bulk before they segregate again at the grain boundaries [21].
As the solubility of Cu seems to be the limiting factor of CdTe doping it is necessary to find ways to increase the solubility. The assumption is that alloying the absorber with Se could lower the defect formation energy and therefore enhance the solubility of the dopant in the bulk. The idea to take Se for this approach is based on first principle calculations done by Jie Ma and Su-Huai Wei in 2013 [15]. They studied the defect formation energy of Cu_{Cd} in CdS_xTe_{1-x} alloys. The result of their calculations was a strong bowing in the defect formation energy shown in Fig. 1.2. The bowing at low Sulfide amounts was explained with the so called strain effect. Because Cu is a small element it induces a compressive strain into the system after forming a Cu_{Cd}. Due to the lattice mismatch between CdS (5.818 Å [27]) and CdTe (6.482 Å [27]) the lattice constant is linearly reduced with increasing S amount (Vegard's law) and therefore reduces this strain and the formation energy decreases. Due to the chemical similarities between Selenium and Sulfide and the big lattice mismatch between CdSe (6.052 Å[27]) and CdTe the same behavior is expected.

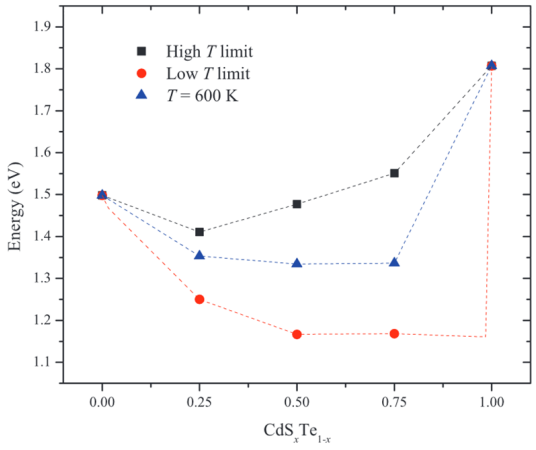

Figure 1.2: *The calculated bowing of the defect formation energy for Cu_{Cd} in CdS_xTe_{1-x} alloys is showed. The energy drops for low amounts of sulfide [15]. The same behavior is expected for $CdTe_{1-x}Se_x$ alloys.*

Another reason for alloying CdTe with CdSe is the band gap bowing effect, which can be used to tune the band gap of the CdTe solar cell by varying the amount of Selenium. The band gap can be shifted closer to the band gap optimum which is 1.34 eV due to calculations based on the Shockley Queisser limit [25] done at Empa. The fitting formula for the band gap bowing of random $CdX_{1-x}Y_x$ alloys is given by: [27]

$$E_g(x) = (1-x)E_g(CdX) + xE_g(CdY) - bx(1-x) \tag{1.1}$$

The factor b is the bowing parameter and for this fitting function the value is 0.75 (first principle calculation from ref. [27]). In other calculations, such as tight binding calculations by [26], the bowing parameter changes to 0.904, and in the Photoluminescence measurements mentioned also in ref. [26] to 0.916. In Fig 1.3 the theoretical band gap bowing for the $CdTe_{1-x}Se_x$ alloy is shown.

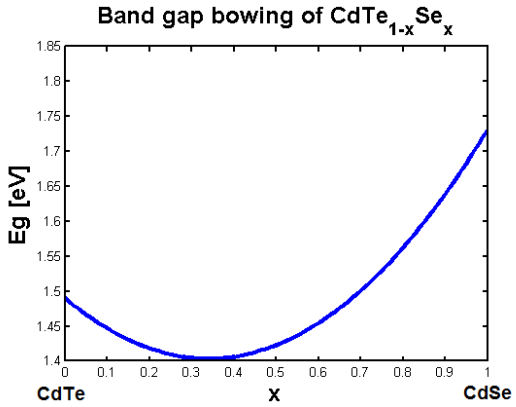

Figure 1.3: *Alloying two semiconductors leads to a band gap bowing. This figure shows a theoretical band gap bowing of the $CdTe_{1-x}Se_x$ alloy calculated with formula* (1.1) *for random $CdX_{1-x}CdY_x$ alloys. The bowing parameter b is 0.75 for this alloy.*

Another problem of CdTe solar cells is a high recombination rate due to a Schottky barrier at the back contact, which lowers the carrier lifetime discussed in Section 2.2.2. In this work incorporation of CdSe at the interface to generate a preferable back surface field was investigated. The idea is based on the possibility of the tunable band gap and calculations based on the tight binding model [26]. These calculations show, with projected density of states calculations, that the influence of the bowing is mainly on the valence band. The prediction in this approach was that with lowering the band gap at the back contact the valence band is locally lifted and this leads to a back surface field for holes without affecting the drift of the electrons in the other direction significantly. This would decrease recombination at the back contact and therefore increase the carrier lifetime.

This thesis consists of three main parts. In the first part the $CdTe_{1-x}Se_x$ alloy is analyzed to determine the influence of CdSe on Cu solubility, band gap and crystal structure. Therefore Hall-, Transmission line- and transmission/reflection measurements, XRD, and SEM were done. In the second part incorporation of Selenium at the interfaces to the back contact and to the CdS layer are investigated. The samples were grown in substrate configuration and analyzed with IV and EQE measurements. In the third part the idea to a new approach came up where the solar cell is based on a p-i-n junction. There the sample configuration was changed to superstrate and the undoped $CdTe_{1-x}Se_x$ alloy acts as the intrinsic layer. This idea is based on experimental results of this thesis. The n-type layer was CdS and as a p-type layer Spiro-OMeTAD and PTAA, which are the hole transporting layer of the Perovskite solar cells[1], were analyzed. The results in this work give a first impression about the properties of the alloy and the p-type layer. The analysis was done by IV and EQE measurements. Since a lot of abbreviations are used in this thesis Appendix A.1 contains a Table that explains the most important ones.

[1] Perovskite is an emerging photovoltaic technology which recently achieved a record efficiency over 20 % at EPFL in Lausanne [1]

2

Theory

2.1 Junctions of a solar cell

A thin film solar cell basically consists of a p-n junction and a front and a back contact. The absorber has a thickness of a few µm and is a p-type semiconductor which absorbs the light to generate electron-hole pairs. By building a junction between the p-type absorber and an n-type window layer the excitons get separated and forced in opposite directions. By building a contact between these to layers their chemical potentials align in thermodynamical equilibrium. This leads to a band bending of the valence and the conduction band. Because the n-type layer contains more electrons and the p-type layer more holes, there is a concentration gradient over the junction resulting in a diffusion current of electrons to the p-layer and holes to the n-layer. This leads to an electric field over the junction. This region is called depletion region. The potential difference over the junction is called built-in potential (V_{bi}), which forces the electrons from the p-type layer to the n-type layer and the holes from the n-type layer to the p-type layer. This is shown in Fig. 2.1 (a). In thermodynamical equilibrium there is no net current because this drift current compensates the diffusion current.
If the junction is illuminated (b) more excited electron-hole pairs in the depletion region or in the p-type absorber get separated by the electric field and the electrons drift into the n layer and the holes into the p layer. In an open circuited system an open circuit voltage (V_{OC}) is built up due to this photon generated drift current (c). If the junction is connected to a wire the current can be discharged and the voltage drops [9].
A variation of the p-n junction is the p-i-n junction. There an intrinsic or undoped layer is introduced between the p- and the n-layer to enlarge the depletion region at the same V_{bi}. This is favorable for layers with a small carrier diffusion length because they are forced in the right direction due to the electric field through the whole layer [14].

2.2 CdTe solar cell in substrate configuration

In this section the properties of the layers of a thin film solar cell will be explained. As an example the standard CdTe solar cell in substrate configuration will be used.

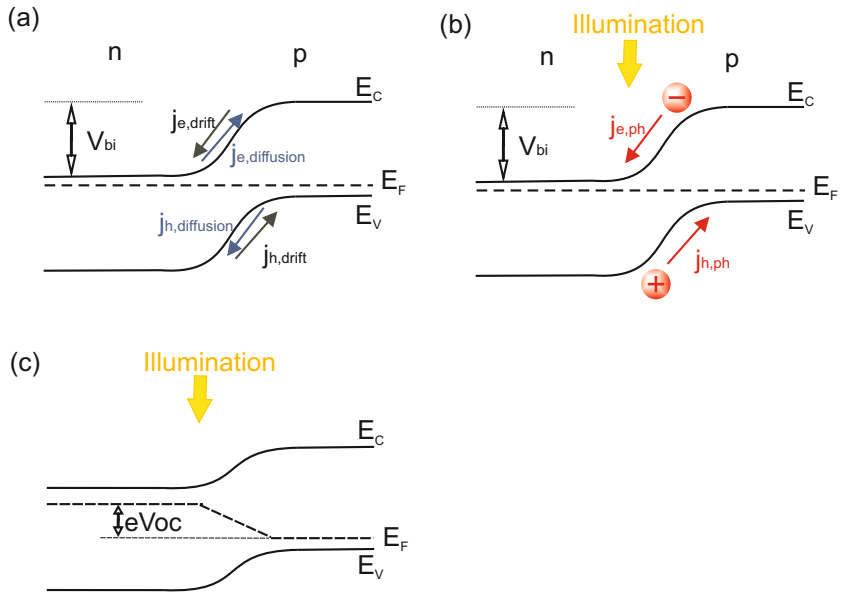

Figure 2.1: *In (a) a p-n junction in thermodynamical equilibrium is shown. Because of the concentration gradient over the junction electrons and holes diffuse to the p-type and to the n-type layer respectively, resulting in an electric field over the junction. The potential difference between the p- and the n-type layer leads to a compensating drift current. If the junction gets illuminated (b) electron-hole pairs are generated which get separated by the electric field over the junction resulting in a photon generated drift current. If the junction is open circuited an open circuit voltage (V_{OC}) is built (c) [9].*

2.2.1 Substrate

Thin films have to be grown on a substrate. If the cells are grown in substrate configuration (Fig.1.1 b), it does not have to be transparent. Used substrates are for example borosilicate glass or flexible metal foil. For CdTe the substrate should not contain sodium, because it diffuses into the sample during the synthesis of the cell.

2.2.2 Back contact

An important part for the discharge of the current in the cell is the back contact. It needs to have a high conductance and should be stable. Another important property is the work function $q\Phi_m$ of the metal. At the interface of the metallic back contact and the semiconductor the Fermi level will align and this leads to a bowing of the bands of the semiconductor. The work function of the metal must therefore be higher than the sum of the electron affinity χ_s and the band gap E_G of the semiconductor to build an ohmic contact for the holes coming from the absorber layer. Otherwise it will form a Schottky barrier. The formula for the height of the barrier $q\Phi_B$ is given by [9]:

$$q\Phi_B = q\Phi_m - (\chi_s + E_G) \tag{2.1}$$

In the case of CdTe with an electron affinity of 4.5 eV and a band gap of 1.49 eV the work function of the material must be greater than 5.8 eV [16]. An additional problem of CdTe are states of the donor like Cadmium vacancies which cause a Fermi level pinning at the interface. This effect leads to a barrier height of 0.8 eV at the interface independent of the metal work function [13]. Therefore it is challenging

to find a proper back contact for the CdTe solar cell and the problem is still not solved. Molybdenum, which is used in this work, fulfills some of these requirements but it has a work function of 4.6 eV and therefore a Schottky barrier for the holes is formed. This is shown in Fig. 2.2 a (before contact) and b (after contact with a Schottky barrier for holes). To overcome the barrier a buffer layer is introduced. The buffer layer has to have a high work function to lower the barrier. Therefore MoO_3 with a work function of about 5.3-6.8 eV is grown on top of the Molybdenum before the deposition of CdTe. This is shown in Fig. 2.2 c. Another possibility is to introduce a highly p-doped buffer layer at the interface to lower the width of the barrier which enhances the tunneling probability for the holes [8].
Nowadays most CdTe cells are grown with a ZnTe buffer layer [28].

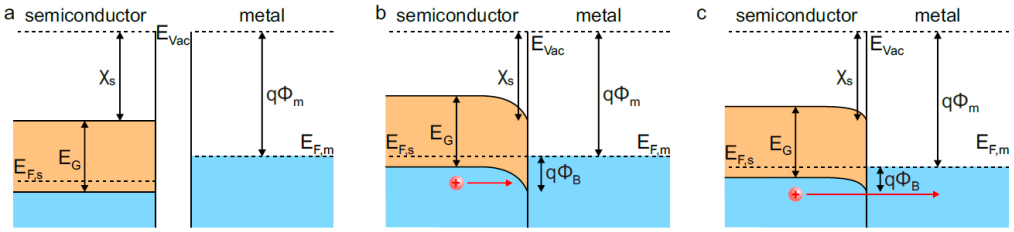

Figure 2.2: *This Figure shows the band bending at the interface of a metal and a semiconductor due to the Fermi level alignment in thermal equilibrium. The situation is shown before (a) and after (b) making contact with the formation of a Schottky barrier. In (c) there is a high work function material between metal and semiconductor which lowers the barrier for the holes [8].*

2.2.3 CdTe absorber layer

The absorber layer is CdTe, a II-VI semiconductor with Cadmium from group two and Tellurium from group four [9]. It has a direct band gap of 1.49 eV at room temperature. The structure is polycrystalline and the grain size depends on the deposition method. For layers made with high vacuum evaporation (HVE), as is used in this work, the grain size is about 0.5 - 1 µm. Its crystal structure is zinc blende and HVE CdTe grows preferentially in the (111) direction. The absorber layer is p-doped, in our case with Copper, to enhance the junction. Additionally Cu is used to reduce the Fermi level pinning mentioned above. To reduce defects and to enlarge the grain boundaries a $CdCl_2$ treatment (see Section 3.2.1) is done. During this treatment, a recrystallization process occurs reducing the (111) orientation and a lot of defects move to the grain boundaries. Additionally the $CdCl_2$ acts as a catalyst for the grain growth. After the treatment the grain size is in the order of the layer thickness [16].

2.2.4 CdS window layer

Solar cells contain a n-type buffer layer between the absorber and the transparent conducting oxide layer (see TCO below.) This layer is necessary to form a proper band alignment in the junction and it helps to reduce defects at the interface which will lead to recombination [16]. Electron hole pairs generated in this layer do not contribute to the current produced by the solar cell because the electric field of the junction rejects the holes and attracts the electrons [18]. This means that the band gap of this material should be as high as possible to reduce absorption. CdS, which is used for CdTe solar cells, is intrinsically n-type [16] and has a band gap of 2.4 eV [11]. After the deposition of this layer a $CdCl_2$ treatment is conducted to recrystallize the CdS layer, increasing its lattice parameter and reducing the lattice mismatch between CdS and CdTe. The Band gap of CdS is 2.4 eV and in the alloy of $CdS_{1-x}CdTe_x$ the band gap minimum of 1.4 eV is achieved at x = 0.25. Another advantage of this treatment is, that Sulfur diffuses into the absorber and helps to passivate the grain boundaries and therefore reduces recombination.

2.2.5 Transparent conducting oxide (TCO)

The challenge for the TCO is, that is has to be transparent for the wavelength range in which the absorber of the solar cell absorbs and simultaneously have a high electrical conductivity. For CdTe this wavelength range is between 300 nm and 850 nm. The most used materials that fulfill these properties are differently doped tin oxides (Fluorine-doped, Indium-doped and Copper-doped) or aluminum doped zinc oxide (AZO) [16]. In this work AZO was used. On top of the TCO a grid is placed to make a contact and discharge the current. To enhance the performance, an anti reflection coating can be deposited on top of the grid and TCO.

2.3 Characterization of thin film solar cells

The methods to characterize solar cells will be explained in this section.

2.3.1 IV Curve

To characterize the main parameter of the solar cell the IV curve is measured. The IV curve of a solar cell in the dark looks like the curve of a diode. With illumination the whole IV curve is shifted downwards because a drift current is generated while absorbing the light [18]. The two IV curves and the corresponding circuits are shown in Fig. 2.3 a and b [10].

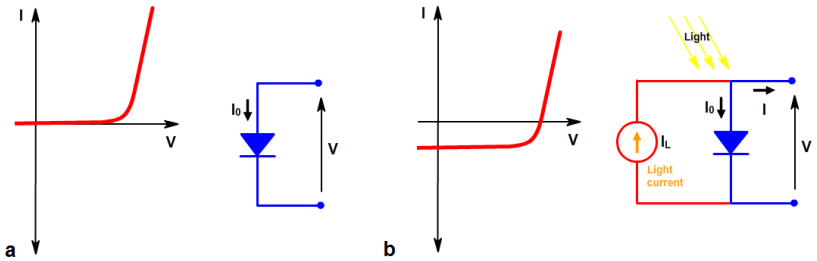

Figure 2.3: *(A) shows the IV curve of a solar cell in the dark with its corresponding circuit. The IV curve looks like a diode. (B) shows a solar cell under illumination. The IV curve shifts downwards and shows the maximum current (I_{SC}) and the maximum voltage (V_{OC}) which are the intersections on the I axis and on the V axis [10] respectively.*

Short-circuit current

As mentioned in Section 2.1, if the solar cell is illuminated there is a current through the solar cell without applying any voltage. The higher the intensity of the illumination the higher the current. The highest current can be obtained at short-circuit conditions (short circuit current). Since the current increases with the number of excited electron-hole pairs, the I_{SC} is higher the lower the band gap of the material. It depends also on the carrier lifetime and the optical properties such as the absorption of the cell material [10]. Since this current also depends on the area of the cell the value is transformed into the short circuit current density J_{SC}.

Open circuit voltage

The potential shown in Fig. 2.1 (c) can be found in the IV curve at the point where the applied forward bias is equal to the bias of the junction with the photon induced current described above. The current through the solar cell is zero at this point. This voltage is therefore called open-circuit voltage and it is the maximum voltage of the cell. The V_{OC} depends on the band gap and on the recombination in the material. The larger the band gap the larger the V_{OC}, and the higher the recombination rate the lower is this voltage [10].

Fill factor

Since the power of the solar cell is zero at the V_{OC} and I_{SC} the so called fill factor is used to determine the maximum power of the cell. It shows the squareness of the IV curve which is depicted in Fig. 2.2. The figure shows an IV curve (red) with the corresponding power curve (blue). The V_{OC} and the I_{SC} are marked on the axes. V_{mp} and I_{mp} are the voltage and the current at the maximum power point P_{max}. The ratio between the two areas A and B gives the fill factor [10].The formula is given by:

$$FF = \frac{I_{mp} \cdot V_{mp}}{I_{SC} \cdot V_{OC}} = \frac{areaA}{areaB} \tag{2.2}$$

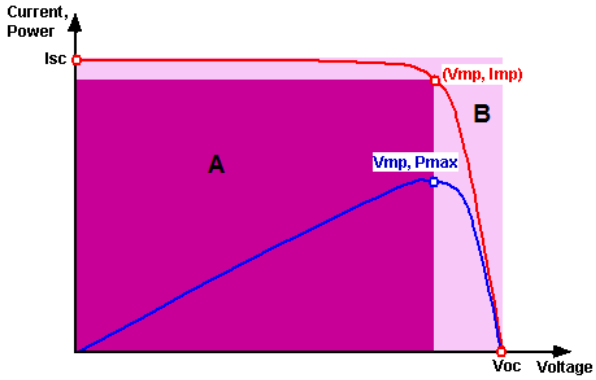

Figure 2.4: *The IV (red) and the power curve (blue) of a solar cell are shown. On the axes the I_{SC} and V_{OC} are marked. V_{mp} and I_{mp} are the voltage and the current at the maximum power point P_{max}. The ratio of the two squares A and B gives the fill factor which represents the squareness of the IV curve and is a measure of the maximum power of the solar cell [10].*

Efficiency

The probably most popular parameter to compare solar cells is the efficiency, which can also be determined by measuring the IV curve. The efficiency η gives the information of how much of the energy of the incident light is converted into electrical energy. It is given by:

$$\eta = \frac{P_{out}}{P_{in}} = \frac{V_{OC} \cdot I_{SC} \cdot FF}{P_{in}} \tag{2.3}$$

where P_{in} represents the power of the incoming light.
The efficiency depends on the spectrum and the intensity of the incoming light as well as on the temperature of the solar cell [10].

2.3.2 EQE

The external quantum efficiency gives the ratio between incoming photons and the number of produced charge carriers that result in a current which can be measured. By varying the wavelength of the incoming photons from blue to red light the range of the absorbed solar spectrum and therefore the band gap and again the J_{SC} can be determined.

3

Experimental methods

In this chapter the experimental methods that are used in this work are explained. First the used substrate is explained shortly. In the second part the setup for the layer deposition methods for the samples in substrate configuration and then for the samples in superstrate configuration are shown. In the third and fourth part the characterization methods for the whole devices and the composition of the absorber layer are explained.

3.1 Substrate

As a substrate Corning 7059 borosilicate glass was used. It was cut in 5x5 cm squares manually with a glass cutting table. To clean the glass it was in a first step washed by hand with deionized water and soap. As a second step it was put in a ultrasonic bath filled with deionized water and soap and then two times in a ultrasonic bath only filled with deionized water.

3.2 Layer deposition methods

3.2.1 Substrate configuration

In this part of the thesis the deposition methods of the layers for the cells in substrate configuration are explained.

Back contact and buffer layer

As a metallic back contact 600 nm of molybdenum was sputtered in a vacuum of about $1 \cdot 10^{-7}$ mbar on the glass substrate. The process was done in an Ar-plasma with a partial pressure in the range of 10^{-3} mbar.
Since there is a Schottky barrier at the interface between Mo and CdTe (see Section 2.2.2), 70 nm of MoO_3 were deposited with high vacuum evaporation (HVE) in a vacuum in the order of 10^{-6} mbar, as a buffer layer. The samples were mounted on a rotating sample holder to achieve a good homogeneity of the layer.

Co-evaporation of the absorber

For the incorporation of the CdSe in the absorber two different techniques were used. The first was co-evaporation.
The CdTe and the CdSe depositions were done simultaneously with HVE. The pressure was around 10^{-6} mbar during the deposition. The setup in the chamber is shown in Fig. 3.1. The CdTe source consists of 4 different openings placed below the four 5x5 cm samples in the sample holder with a distance of 12 cm. On top of it the CdSe source is installed, thermally insulated from the CdTe source with an molybdenum plate. Both sources can be heated separately with individually applied currents. The sample holder is held constantly at 350 °C.
To determine the amount of Se in the $CdTe_{1-x}Se_x$ alloy and also to determine the thickness of the whole absorber two quartz microbalances are installed in the chamber. One quartz microbalance is on the same height as the samples facing downwards to control the rate and the amount of material deposited on the samples. The second quartz microbalance is installed next to the CdSe source holder facing to the source. In front of it there is an molybdenum sheet with a slit of 5 mm to reduce the amount of CdTe measured by this quartz microbalance. In total there were around 5 µm deposited on the samples. The deposition of the $CdTe_{1-x}Se_x$ alloy is followed by a $CdCl_2$ treatment (see Section 3.2.1 below).

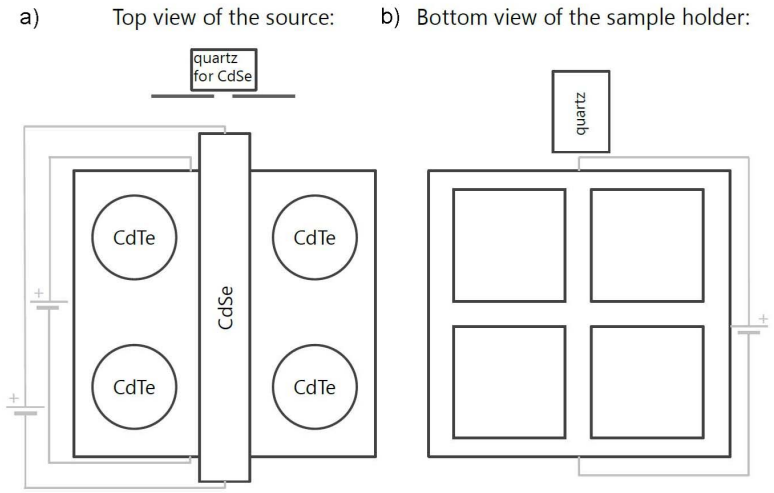

Figure 3.1: *In (a) the schematic setup of the CdTe and the CdSe source is shown. The source holder of CdTe consists of four round openings in an Mo sheet and the CdTe is placed below this sheet in a heatable boat. Above there is the rectangular, separately heatable boat filled with CdSe. Next to the CdSe source a quartz microbalance is placed to measure the evaporated amount of CdSe. To reduce the amount of CdTe on this quartz microbalance a molybdenum sheet with a slit of 0.5 cm is placed in front of the quartz. (b) shows the bottom view of the heatable sample holder. Four samples can be placed above the CdTe openings with a distance of 12 cm. On the same height another quartz microbalance is installed to measure the total amount of the evaporated material on the samples.*

With this method samples of x = 0 - 0.5 with a thickness of 5 µm were made to investigate the crystal structure, grain size and the band gap of this alloy. This was done with XRD (Section 3.4.2), SEM (Section 3.4.3), and with transmission/reflection measurements (Section 3.4.5).

In a second step samples with x varied from 0 to 0.20 with a thickness of 10 µm were made to measure the resistivity with Van der Pauw and transmission line measurements, and the carrier density and mobility

with the Hall effect measurements (see Section 3.4.7 and Section 3.4.6). In these samples also the grain size was investigated with top view SEM images and analyzed with the program ImageJ. In these samples the annealing temperature was varied from the standard of 435 °C to 450 °C.

Another aspect of this method was to look at the influence of CdSe on the interface to the back contact. Therefore whole cells were made with varied absorber compositions. The absorber consisted of 500 nm $CdTe_{1-x}Se_x$ and 4.5 µm pure CdTe, with x = 0, 0.1, 0.2 and 0.25. All other layers were done with their standard deposition method.

Two- or three-step evaporation of the absorber

With this technique the CdTe layer was deposited in the same chamber as the co-evaporation method but the CdSe deposition was done in another chamber without substrate heating. Three different methods can be applied. The CdSe layer is deposited before the CdTe layer, afterwards, or both. In this thesis only the method with CdSe evaporated on the already deposited CdTe layer was analyzed. This step was followed by the $CdCl_2$ treatment described below which leads to a intermixing of the compounds. With this method the CdSe will diffuse up to 1 µm into the CdTe layer [20].
This technique was executed to investigate the influence of CdSe at the interface to the window layer. Therefore whole cells were made with varied thickness of the evaporated CdSe layer. The experiment was done with 50 nm, 100 nm, 150 nm and 200 nm CdSe on 5 µm CdTe.

Doping

To p-dope the material 1.2 Å Copper was evaporated with HVE on top of the absorber. After the deposition the samples were annealed at 400 °C for 20 min in a 200 mbar O_2 and 300 mbar Ar atmosphere. The Cu atoms diffuse into the absorber material and a homogeneous Cu distribution can be achieved. After the solar cell was finished the cell was again annealed for 10 min in air at 210 °C and then quenched by rapid cooling on a Copper plate to enhance the amount of free charge carriers.
To investigate the influence of CdSe on the charge carrier concentration, resistivity and mobility the amount of 1.2 Å was varied from 1 to 8 Å.

Window layer

The window layer CdS was deposited with chemical bath deposition (CBD) on top of the CdTe absorber. Since the lattice mismatch between CdS and CdTe is too large this deposition has to be done twice. After the first CBD and a drying time of two days, a $CdCl_2$ treatment (see below) has to be done to enlarge the lattice parameter of CdS. Then the second CdS layer was deposited. As a standard recipe the deposition was done for 18 min which corresponds to 60 nm CdS on the sample. The bath was placed in a 70 °C water tank and consisted of 200 ml deionized water, 15 ml Cadmium Acetate, 15 ml Thiourea and 25 ml Ammonium Hydroxide.
To investigate the influence of CdSe on this layer the CBD deposition time was varied to 1x12 min, 2x12 min, 1x15 min, 2x15 min and 1x18 min for samples with 50 nm Selenium deposited with the two-step evaporation method.
At the end of this thesis some 60 nm thick CdS:0 window layers were investigated with sputtered CdS in the Sputter Cluster CT200. The Argon flow was for each deposition 66 sccm. The Oxygen flow was varied from 0, 2, 3 and 4 sccm. The power of the radio frequency was 120 W. The first step of this experiment was to replace the second CBD, and then replace both CBDs also with a $CdCl_2$ treatment

between them. In a third step 120 nm and 60 nm sputtered CdS:O layers followed by a $CdCl_2$ treatment were done. It is important to mention that the possibility of sputtering CdS is new and the process is not yet optimized.

$CdCl_2$ treatment

As mentioned above the $CdCl_2$ treatment is an important step in processing the solar cells. An amount in the range of a few nm of $CdCl_2$ is deposited on the layers with HVE and then the whole sample is annealed for 25 minutes.
In the treatment of the absorber 400 nm of $CdCl_2$ were deposited and the annealing took place at 435 °C for 25 minutes.
The treatment after the first CBD was done with a 100 nm $CdCl_2$ deposition and the annealing took place at 360 °C for 25 minutes.
The annealings were done in an Ar and O_2 atmosphere.

Front contact

The front contact consisted of an intrinsic ZnO (IZO) and an Aluminum doped ZnO (AZO) layer deposited with high frequency sputtering and a nickel aluminum grid. 50 nm Ni and 4 µm Al were evaporated with electron beam evaporation. Up to 49 grids were placed on each 5x5 cm sample.
To separate all these 49 cells, the sample had to be scribed. This was done manually with a sharp thin knife, like a scalpel, and a ruler. The scribing goes through all the layers except the back contact.

3.2.2 Superstrate configuration

In superstrate configuration the whole structure explained above is inverted. In this work the new approach of a p-i-n junction is analyzed wherefore an additional layer is introduced.

Front contact and window layer

To contact the TCO after finishing the cell, instead of the grid in substrate configuration, two strips of 300 nm Al and 50 nm Ni were evaporated on two sides of the glass substrate with e-beam evaporation. After depositing all the layers, on these two sides the cells were scratched down to these strips with AcN. With the Sputter Cluster CT200 the transparent oxide layer with 1 µm of AZO and 50 nm IZO was sputtered on the glass with the Al strips by Lukas Greuter. After the deposition it was annealed at 450 °C for 30 minutes in vacuum.
To deposit the n-type layer 200 nm CdS were sputtered in Ar atmosphere also with the Sputter Cluster CT200 by Alex Claville Lopez. The power of the RF was 120 W and the pressure was 10^{-3} mbar. Some samples were annealed after the CdS deposition at 420 °C for 30 minutes in vacuum.

Intrinsic layer

As an intrinsic layer 0.5 or 1 µm of the $CdTe_{1-x}Se_x$ alloy was grown with the co-evaporation technique described above, with x = 0.15, 0.20, 0.25. As a next step a $CdCl_2$ treatment was done with 100 nm

$CdCl_2$ deposited on the alloy followed by an annealing at 460 °C for 25 minutes. In the last experiment of this approach the temperature was varied from 400 to 430 °C in steps of 10 °C.

P-type layer

The deposition of the p-type layer was done with spin coating in a nitrogen atmosphere by Fan Fu and Stefano Pisoni. The working principle is to coat the sample with a solution, containing the molecules of the material to deposit, and a solvent. The solution will flow to the side when the sample is rotating. Due to the airflow, the solvent dries and just leaves the molecules on the sample with a homogeneous distribution.
Different compositions of Spiro-OMeTAD and PTAA were investigated. PTAA and Spiro-OMeTAD are polymers with valence band energy levels of -5.1 eV (PTAA) and -5.2 eV (Spiro-OMeTAD) [4] (The one of CdTe is at -5.2 eV [23]). Their whole names are listened in Table A.1 and the composition of the solutions can be found in the Appendix A.2. The first experiments were done with dynamic spin coating, where the solution is pipetted on rotating sample, and then with static spin coating, where first the solution is placed on the sample and then the rotation is started. The parameters which determine film thickness and homogeneity are spin speed, duration time and the concentration of the molecules dissolved in a solvent [19]. The parameters used in this work are shown in Table 3.1. The concentration of the solution was not varied but the amount of the solution deposited on the sample.

Table 3.1: *In this table the investigated spin coating parameters are shown.*

Spin coating method	Amount [µl]	Spin speed [rpm]	Spin coating duration [s]
dynamic	25	2000	40
static	100	2000	40
static	100	1000	40
static	100	500	40

Three experiments were done. In the first run Variation A for PTAA and Spiro-OMeTAD was used on a $CdTe_{1-x}Se_x$ alloy with x = 0.20. In the second run all 4 methods were compared on an alloy with x = 0.25 and in the third run variation A only with PTAA was used on alloys with x = 0.15 and 0.20.

Back contact

As a back contact gold was deposited with HVE. The samples were placed on a mask with rectangles with an area of 0.15 cm^2. Due to this mask the cells were already defined and no scribing was necessary.

3.2.3 In situ and ex situ thickness control

To control the layer thickness and the rate during the layer deposition crystal quartz microbalances were used.
After the deposition the layer thickness was determined with a high resolution surface profilometer (AM-BIOS XP1). A diamond stylus in contact with the surface scans the sample. The height change of the stylus gives the thickness of the layers.

3.3 Device characterization

3.3.1 IV Curve

To characterize the performance of the cell the IV curve of the finished cell was measured. The cell sizes were determined by scanning the samples and measuring the scribed areas with the program GIMP. The applied voltage was varied in the range of -1 to 1 V and the current through the solar cell was measured. To compare the measured values every laboratory has to measure under standard test conditions. To reproduce the standard test conditions the incoming photons are generated with the solar simulator *LOT-QD LS0811* with the photon spectrum for 1.5AM. The power of the photons on the cell is 1000 W/m^2 and the temperature of the sample was stabilized at 25 °C. To control the standard test condition a silicon based reference cell calibrated by the Fraunhofer Institute for Solar Energy Systems was used. For some of the p-i-n junction cells a special setup with a heat stabilized Sapphire window was used.

3.3.2 External quantum efficiency (EQE)

To determine the quantum efficiency of each cell EQE measurements were done. The light source for the EQE measurement was a chopped white light source with a chopper frequency of 260 Hz and a power of 900 W. The wavelength of the incoming photons was varied from 390 nm up to 1000 nm in steps of 10 nm. The reference cell for the calibration of each measurement was a silicon based cell calibrated by the Fraunhofer Institute for Solar Energy Systems. These measurements were also done to determine the band gap and the J_{SC} of the p-i-n junction cells.

3.4 Characterization of the composition

3.4.1 X-ray fluorescence (XRF)

To make a first analysis of the sample composition X-ray fluorescence measurements were done with the PANalytical X'Pert Pro MPD X-ray Diffractometer. The acceleration energy of the incident photons was 45 kV. These high energy photons knock out core electrons and higher shell electrons will take their places by losing energy in form of photons that are detected. This results in a characteristic x-ray spectrum.

3.4.2 X-ray diffraction (XRD)

XRD measurements were done with the Siemens D5000 X-Ray Diffractometer with the help of Stefan Haass to analyze the crystal structure of the alloyed samples. The angle 2θ was varied from 20°to 80°. The photons were extracted of a Cu-anode (λ_{k_α} = 1.5406 Å) with an acceleration voltage of 40 kV.

XRD measurements are based on interference of elastically scattered photons at atoms. The atoms are arranged in lattice planes with a distance d between them as shown in Fig. 3.2. The beam with an incidence angle θ scatters at the atoms in the planes and the elastic scattered ones enters the detector under the same angle θ. The distance between the lattice planes can be calculated with the Bragg equation (3.1) where λ is the wavelength of the incoming photon beam and hkl are the Miller indices of the lattice planes.

$$2 \cdot d_{hkl} \cdot sin(\theta_{hkl}) = \lambda \tag{3.1}$$

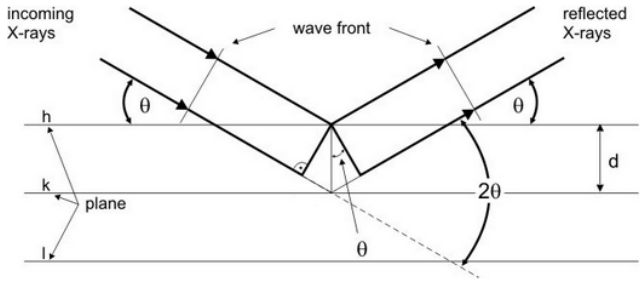

Figure 3.2: *In this Figure the lattice planes of a crystal are shown. If X-rays of a small wavelength at a certain angle θ scatter elastically at the atoms, they leave the lattice under the same angle. The Figure was extracted from reference [5].*

The peaks depend amongst others on the lattice parameter, grain size, phase composition and preferred orientations. For example the smaller the grain size the broader the peak or the more preferred an orientation the higher the intensity of the peak. The position of the peak depends on the lattice parameter [24].

3.4.3 Scanning electron microscope (SEM)

With the Hitachi S-4800 Field Emission - and the Nova NanoSEM 230 FEI Scanning Electron Microscope, secondary electron microscopy was done to analyze the layers. The acceleration voltage of the incoming electrons was 5 kV and the working distance was about 4 mm for cross section images and about 4-6 mm for top view images. The cross section images were done by Stefano Pisoni to look at the coverage of the p-type layer of the p-i-n junction cells. The top view images to determine the grain size were done by Martina Lingg. These samples were etched with 0.1 % bromine in methanol for 4 seconds before obtaining SEM pictures. The analysis of the grain size was done by using the program ImageJ.

Energy dispersive x-ray spectroscopy (EDX)

To analyze the composition of the absorber material EDX was used. The electrons coming from the electron gun of the microscope were accelerated with a voltage of 20-30 kV while scanning. To verify changes in the material composition over the cross section of the sample line scans with several measuring points over the cross section were done. The working principle of EDX measurements is similar to the XRF. High energy electron are able to knock core electrons out of the atoms in the sample. An electron from a higher energy level in the atom will lower its energy by emitting an x-ray and taking the empty state of the knocked out electron. This results in a x-ray spectrum consisting of Bremsstrahlung and characteristic peaks. With those peaks the elements in the bulk can be determined [2].

3.4.4 Inductively coupled plasma optical emission spectrometry (ICP-OES)

To determine the exact composition in the samples ICP-OES was done. These measurements were done by the Laboratory for Advanced Analytical Technologies at EMPA Dübendorf. The samples were dissolved in HNO_3 67 %, H_2O_2 30 % and deionized water at room temperature. After 10 minutes the solution was diluted with deionized water. The solution was injected into an inductively coupled Ar plasma where the atoms get ionized and excited. Due to the excitation the ions emit photons which are detected by a polychromator that filters the wavelength.

3.4.5 Transmittance and Reflectance

To estimate the band gap of the alloys transmittance and reflectance measurements were done with the UV 3600 UV-VIS-NIR Spectrophotometer Shimadzu. The wavelength was varied from 300 nm to 1100 nm in steps of 2 nm. For the calibration baseline measurements were done with $BaSO_4$ plates for background.

3.4.6 Hall measurements

To measure the resistivity the Van der Pauw method was used. The samples had a thickness of 10 µm and were scribed to get a square geometry with a side length of 8 mm. As contacts four 50 nm thick gold squares were evaporated on the sample edges. The amount of CdSe in the alloy and the amount of Cu as dopant were varied. The measurements were performed at 70 °C controlled with a peltier element. To determine the hall coefficient the same setup with a magnet of 0.58 T was used. The hall voltage is measured at -0.58 T and 0.58 T.

3.4.7 Transmission line measurements (TLM)

Transmission line measurements are another method to determine the resistivity. The same samples as in the Hall measurements were used but instead of the gold squares at the edges line shaped gold contact with varying distances are deposited. The line shape was achieved with a mask. Over each distance the resistance is measured and then it is plotted against de distances between the contacts to calculate the resistivity from the slope as shown in Fig. 3.3. The measurements were done in darkness.

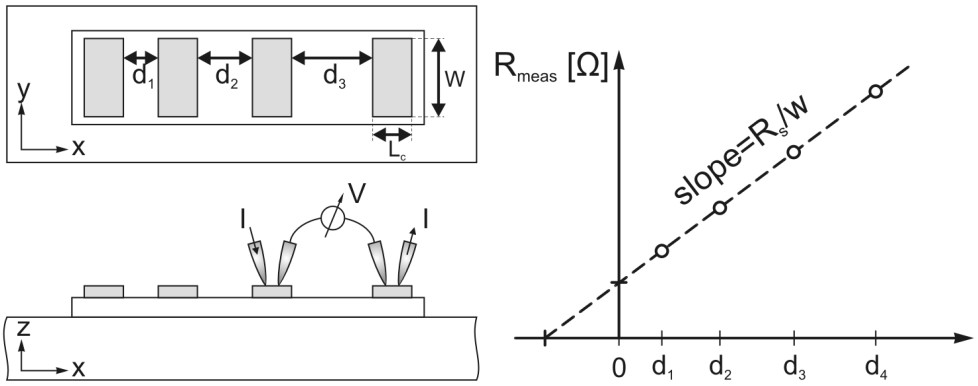

Figure 3.3: *The experimental set up to measure the resistance over two contacts with different distances (left) and the graph to determine the resistivity of the sample (right) are shown. Line contacts are deposited in different distances on top of the sample and the resistance between each distance is measured. To get de resistivity the measured resistances (R_{meas}) are plotted against the distances between the contacts. The resistivity can be calculated from the slope of this graph, the contact length and the sample thickness. The figure is extracted from [17]*

4

Results and Discussion

The results are presented in two parts. In the first part the measurements of the samples grown in substrate configuration will be shown and discussed. In the second part the new superstrate approach will be analyzed.

4.1 Results of measurements in substrate configuration

4.1.1 Results of the ICP-OES

During the co-evaporation of CdTe and CdSe the rate was controlled by two quartz microbalances explained in Section 3.2.1. To determine the exact composition ICP-OES measurements were done. In these results the error of $\pm$ 2% is introduced because it is shown that the ratio of Selenium to Tellurium varies around $\pm$ 2% over the area of a sample. This variation over the sample is because of the source setup used for the co-evaporation method explained in Section 3.2.1. On Table 4.1 the mean values of the samples are shown and compared with the expected x from the evaporation. (On Table A.2 in the Appendix the example for x = 0.2 is shown.) The Selenium amounts agree with the expected values.

Table 4.1: *The measured amount of Selenium is compared with the expected amount from the co-evaporation.*

at% Selenium	at% Tellurium	x ICP-OES	Expected x
4 ± 2	45 ± 2	0.08 ± 0.02	0.10
10 ± 2	39 ± 2	0.20 ± 0.02	0.20
14 ± 2	35 ± 2	0.27 ± 0.02	0.30
19 ± 2	30 ± 2	0.38 ± 0.02	0.40
24 ± 2	25 ± 2	0.49 ± 0.02	0.50

The analyses where the values are corrected are marked. Otherwise the expected Selenium amounts are written down.

4.1.2 Effect of Selenium on the grain size

To investigate the grain size of the $CdTe_{1-x}Se_x$ absorber top view SEM images were made and analyzed. Fig. 4.1 shows that the grain size decreases with increasing amount of Se. With increasing the $CdCl_2$ treatment annealing temperature the grain sizes increase.

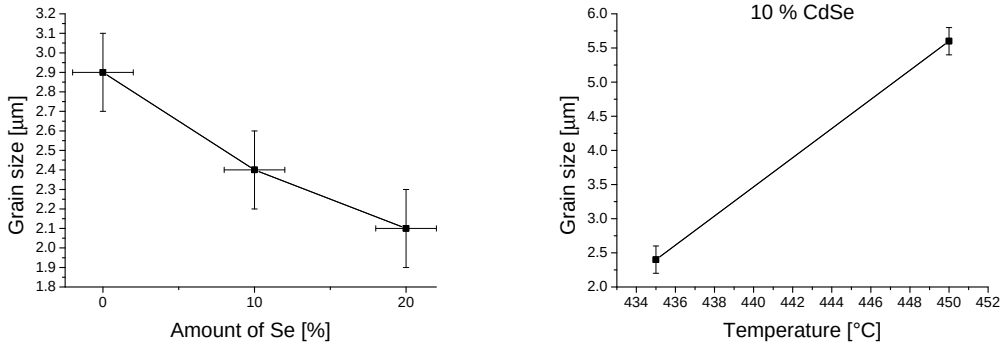

Figure 4.1: *On the graph on the left the effect of Selenium on the grain size is shown. It decreases with increasing amount of Selenium. On the right hand side it is shown that the grain size increases again if the annealing temperature of the $CdCl_2$ treatment is increased.*

4.1.3 Results of the Hall and transmission line measurements

Samples of a $CdTe_{1-x}Se_x$ alloy with a CdSe content of x= 0, 0.1 and 0.2 on glass were measured to determine the influence of CdSe on charge carrier concentration, mobility and resistivity. The samples were heated to 70 °C for the Hall measurements. The TLM measurements were done at room temperature in darkness. For more details see Section 3.4.6 and Section 3.4.7. The results are plotted against the different Cu amounts in the samples and are shown in Fig. 4.2. The influence of the increased $CdCl_2$ treatment annealing temperature is shown on Fig. 4.3. The resistivity decreases with increasing annealing temperature.

The Hall measurements show that the charge carrier density is reduced with a higher amount of CdSe and the resistivity of the sample is increased. The mobility is in the same order of magnitude. The TLM measurements at room temperature in darkness also show an increased resistivity with increasing amount of CdSe.

4.1.4 Band gap bowing

The influence of CdSe on the band gap of the absorber was investigated with transmission/ reflection measurements. The samples consisted of 5 µm thick $CdTe_{1-x}Se_x$ alloys on glass with a $CdCl_2$ treatment. The amount x of Se was varied from 0 tu 0.5. The Tauc plot was calculated from this data to determine the band gap by fitting its linear part. This is shown in Fig 4.4. In Fig.4.5 these band gaps are plotted against the corresponding amount of Selenium x, corrected with the results from ICP-OES measurements, and then fitted with a polynomial fit. The coefficient squared is equivalent to the bowing parameter of the measured data. The band gap for pure CdSe at x = 1 is from literature. The error on the x axis is due to the inhomogeneity of the Selenium over the sample.

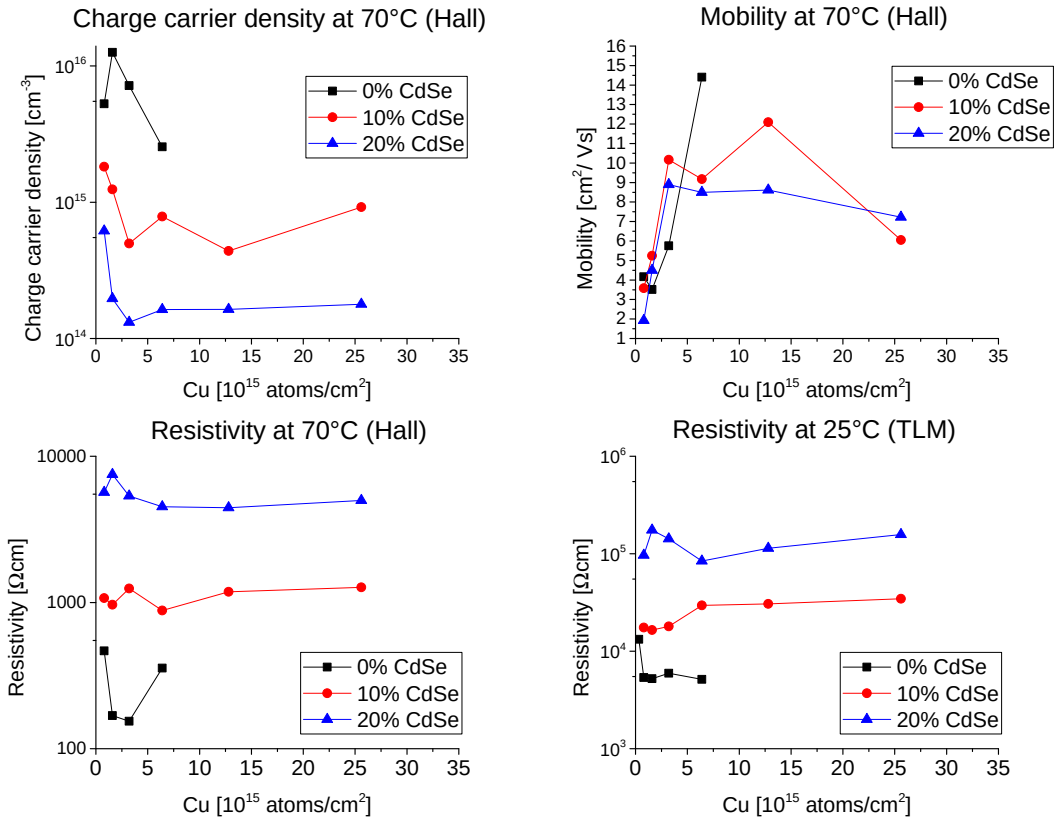

Figure 4.2: *Results of Hall and TLM measurements are plotted against different Cu amounts in the samples. They show that the charge carrier concentration is reduced with increasing CdSe and the resistivity is increased. The mobility is in the same order of magnitude.*

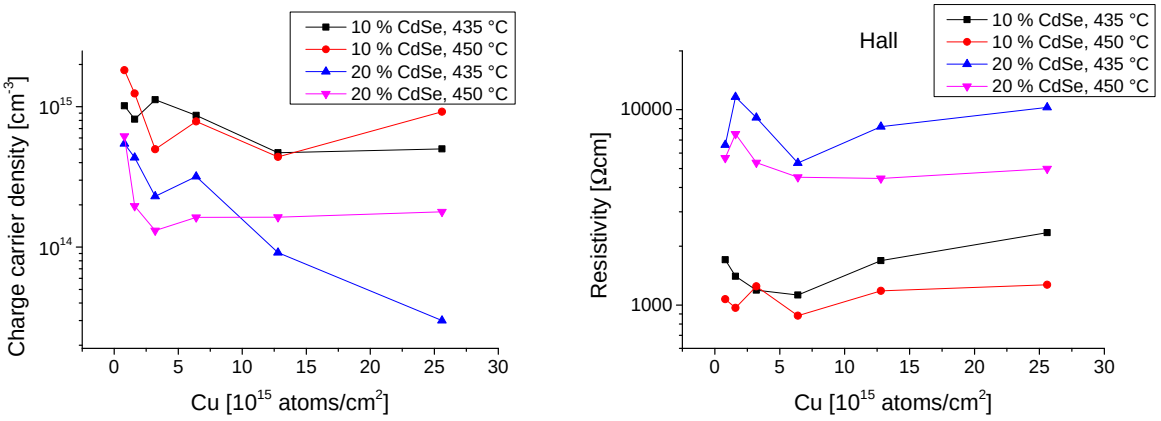

Figure 4.3: *Hall measurements were conducted of samples with $CdCl_2$ treatment annealing temperatures of 435 and 450. One can see a decreasing of the resistivity if the annealing temperature of the $CdCl_2$ treatment is increased. The charge carrier concentration stays in the same order of magnitude.*

Fig. 4.5 shows the band gap bowing of the alloy with a bowing parameter of 0.78 from the fit. The measured data agree with the theoretical bowing from first principle calculations [27] (see Chapter 1). The minimum value of the fit is at x = 0.38 with a band gap of 1.40 eV.
Additional to the shift in the band gap a difference in the slope of the absorbance is visible in the Tauc plot in the samples with Selenium amount higher than 20 %.

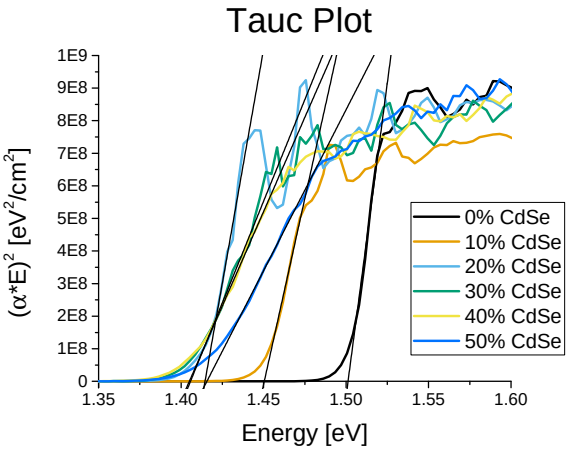

Figure 4.4: *This figure shows the Tauc plot of transmission reflection measurements of $CdTe_{1-x}Se_x$ alloys. The linear part is fitted to determine the shift in the band gap.*

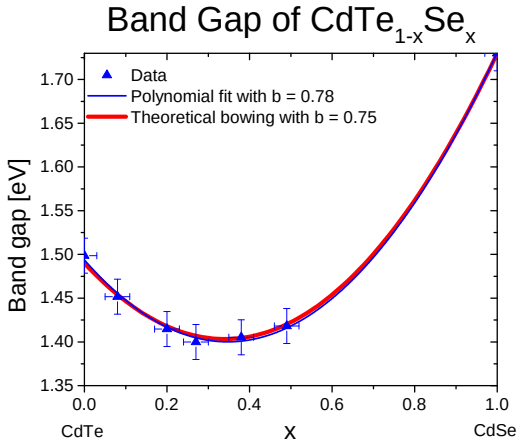

Figure 4.5: *The band gaps determined from the Tauc plot are plotted against the amount of Selenium in the sample (corrected x values). The data points are fitted with a polynomial fit to determine the bowing parameter. The data point of x = 1 is from literature. The measured data agree with the theoretical bowing.*

4.1.5 Layer composition and phases (XRD)

The crystal structure of the $CdTe_{1-x}Se_x$ alloy was investigated with XRD measurements. Rocking curves of samples with Selenium content x = 0 to 0.5 were measured and compared with reference patterns obtained from the ICSD - XRD database Karlsruhe[1] and can be found in Ref. [22] and [29]. Up to x = 0.4, the samples show the cubic zinc blende structure of pure CdTe with a shift to higher angles at higher x. In Fig. 4.6 all measurements are compared to investigate the shifts of the most pronounced peaks. As discussed in Section 2.2.3 the preferred growth direction of high vacuum evaporated CdTe is the (111) direction. The shift of the peaks are taken to investigate the lattice parameter of $CdTe_{1-x}Se_x$. The lattice parameter was calculated with the Bragg equation and the angles of the peaks and plotted in Fig. 4.7 against the amount of Selenium. The shift in the lattice parameter follows Vegard's law.
In Fig. 4.8 a section of the samples with x = 0.4 and 0.5 is shown to determine the influence on the crystal phases. The peaks are compared with reference points of pure CdTe and pure CdSe. An additional peak between the shifted CdTe (220) and (311) peaks is visible in the x = 0.5 sample.

[1] CdTe: collection code: 93942, CdSe: collection code: 41491

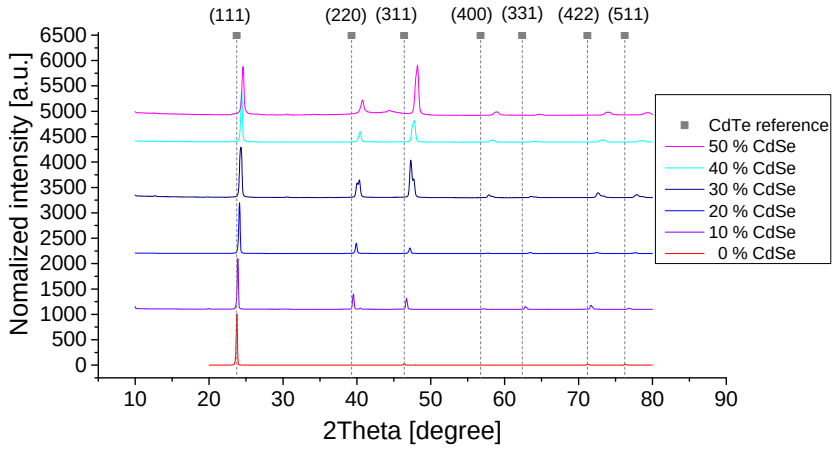

Figure 4.6: *XRD of the $CdTe_{1-x}Se_x$ alloys with x varied from 0 to 0.5 was measured. The most outstanding peaks are compared with a CdTe reference to investigate their shift with different amount of CdSe.*

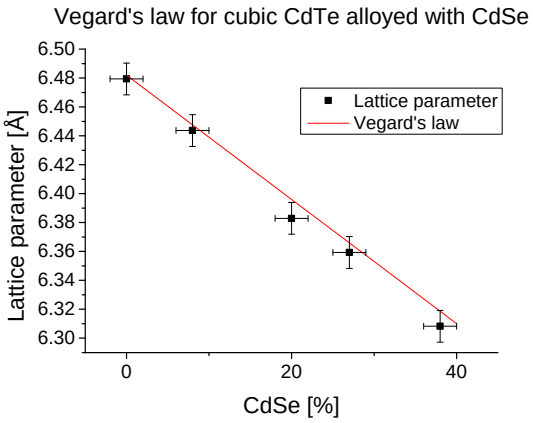

Figure 4.7: *With the Bragg equation and the angles of the peaks, the lattice parameter was calculated and plotted against the amount of CdSe (corrected x values) in those samples. The results agree with Vegard's law.*

4.1.6 Selenium at the back contact

Incorporation of Selenium at the back contact was investigated to determine the influence on the IV parameters. Therefore at the beginning of the absorber deposition 500 nm were co-evaporated (see Section 3.2.1) with different amount of CdSe. The rest of the absorber was pure CdTe. For all other deposition steps the standard techniques were used. IV and EQE measurements of the finished cells were done. The results are shown on Fig 4.9.

The J_{SC} is enhanced with higher amount of Selenium but the V_{OC} and FF are reduced and also the efficiency drops.

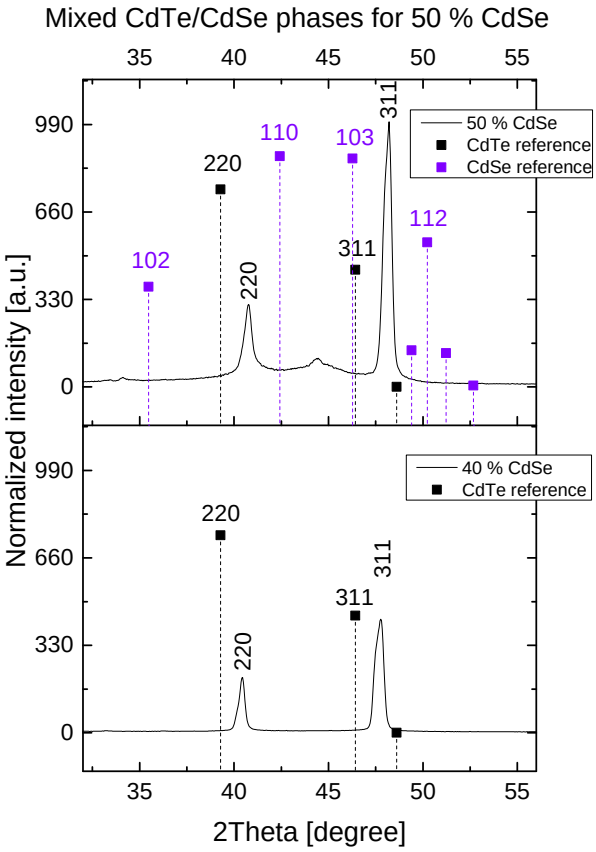

Figure 4.8: *A section of the XRD spectrum of the samples with 40 % and 50 % is shown. The most pronounced peaks are compared with reference points of pure CdTe and pure CdSe. It is shown that an additional peak shows up in between the 220 and 311 CdTe peaks for the sample containing 50 % CdSe.*

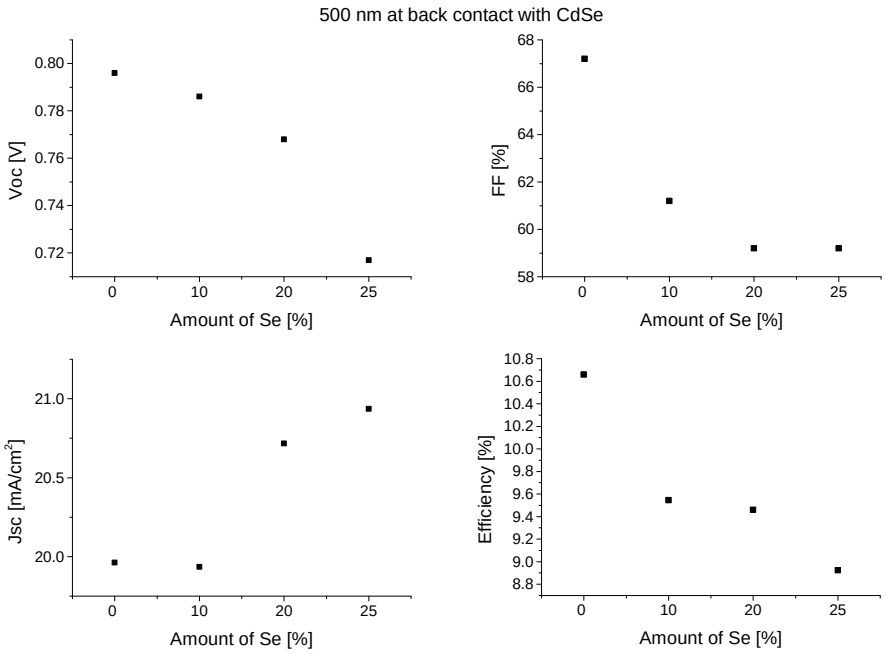

Figure 4.9: *In this Figure the influence of CdSe at the interface to the back contact on the IV parameter is shown. The V_{OC} and FF decrease with increasing amount of Selenium while the J_{SC} increases. The efficiency decreases.*

4.1.7 Selenium at the junction

Incorporation of Selenium at the CdTe/CdS interface was also investigated to determine the influence on the IV parameters. Therefore 50 to 200 nm CdSe were deposited on top of 5 µm CdTe before the $CdCl_2$ treatment. As in the case for the back contact EQE and IV measurements were done. The deposition time of the CBD of these samples was 2x12 minutes, all other depositions were done by the standard techniques. It is shown that at lower amounts of Selenium the J_{SC} increases but drops again at higher amounts. V_{OC}, FF and efficiency decrease with increasing amount of Selenium

CdSe can have an influence on the lattice mismatch between CdTe and CdS (see Chapter 1). The $CdCl_2$ treatment of the CdS layer increases the lattice parameter of CdS. Because CdTe alloyed with CdSe reduces the lattice parameter of CdTe, it was investigated if this treatment still is necessary. Fig. 4.11 shows that the V_{OC} is reduced without this treatment but the J_{SC} and the FF increase. At low amounts of Selenium the overall performance is not influenced significantly but at higher amounts it decreases.

Table 4.2: *On this table the IV parameters corresponding to the IV curves in Figure 4.11 are listed.*

	IV parameter			
Sample variation	**V_{OC} [V]**	**J_{SC} [mA/cm^2]**	**FF [%]**	**Efficiency [%]**
0.5 % CdSe, w/ treatment	0.791	20.46	60.3	10
0.5 % CdSe, w/o treatment	0.739	21.32	66.2	10.5
1.0 % CdSe, w/ treatment	0.816	20.06	64.6	11.2
1.0 % CdSe, w/o treatment	0.732	20.93	66.3	10.5

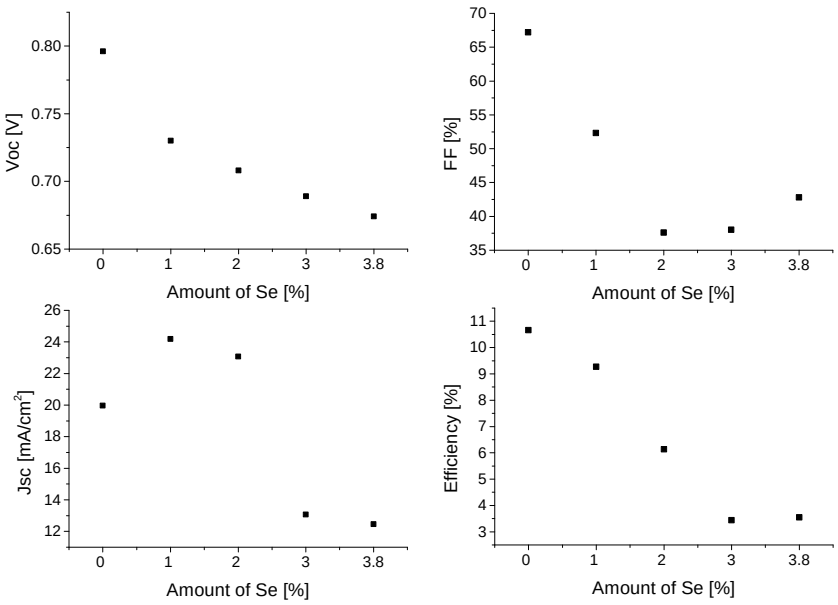

Figure 4.10: *This Figure shows the IV parameters of samples with different CdSe amounts at the interface to the junction. The amount of CdSe is varied by depositing layers of different thicknesses of CdSe on top of 5 µm CdTe just before the $CdCl_2$. It is shown that the V_{OC} and the FF decrease but the J_{SC} increases at low amount of Selenium. The efficiency decreases with increasing amount of Selenium.*

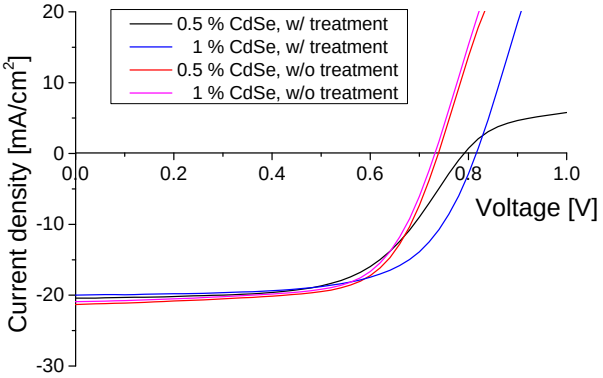

Figure 4.11: *The Figure shows the IV curves of samples with 0.5 % and 1 % Selenium at the interface to the junction. It can be seen that the V_{OC} shifts to lower values without the treatment. The J_{SC} is enhanced.*

4.1.8 Effect of Selenium on CdS and CdS:O

To investigate the influence of CdSe on the interface to the window layer, samples with 50 nm CdSe deposited on 5 µm CdTe were done with the 2 step evaporation method explained in Section 3.2.1. In a first step CdS layers were deposited by CDB with durations of 2x12 and 2x15. Between the two depositions a $CdCl_2$ treatment was done (see Section 3.2.1). Additionally samples with 1x12, 1x15 and 1x18 minutes with a $CdCl_2$ treatment were done. In Fig. 4.12 the parameters determined by the IV measurements of the finished cells (see Section 2.3.1) are plotted against the deposition time. The reference value corresponds to a pure CdTe cell with the standard CdS CBD deposition of 2x18 minutes.

18 minutes result in a 60 nm CdS layer. The points at 24, 30 and 36 minutes corresponds to the 2x12, 2x15 and 2x18 minutes. The V_{OC} decreases with decreasing deposition time while the J_{SC} is increased. FF and efficiency stay in the same order of magnitude as the reference cell.

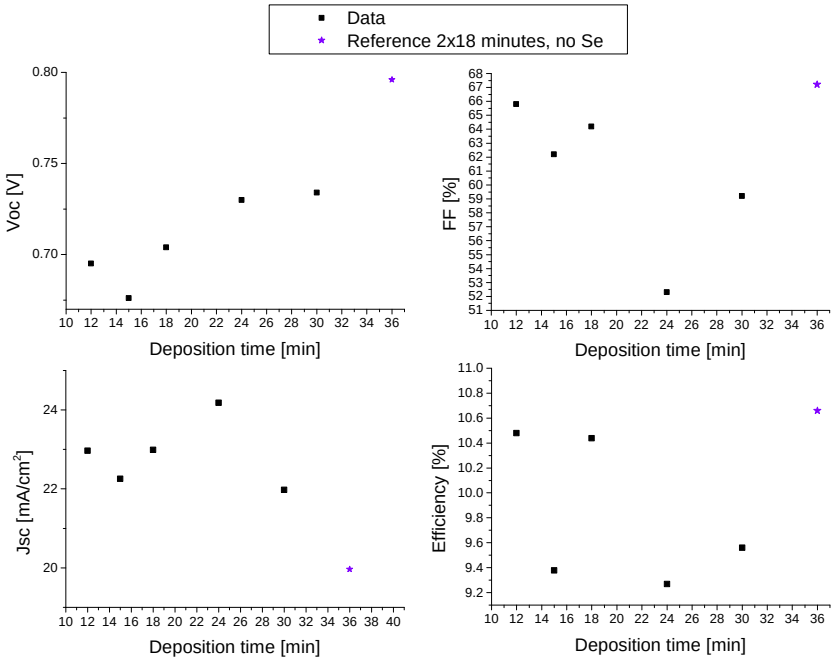

Figure 4.12: *In this Figure the parameters determined by IV measurements are plotted against different CBD deposition times of the CdS layer. The reference point corresponds to a sample without CdSe and the standard CdS deposition. The V_{OC} increases with the deposition time. The J_{SC} is higher than the current density of the reference cell. At short deposition times FF and efficiency are in the same order of magnitude as the reference cell but drop at higher deposition times.*

In a second step oxygenated CdS was deposited with radio frequency sputtering. The CdS layers deposited by CBD were partially or completely replaced by sputtered CdS:O. Partial replacements means that the first CdS layer was deposited by CBD and the second layer by sputtering. The plasma was a mixture of argon and oxygen. The amount of argon was stabilized at a gas flow of 66 sccm and the investigated amounts of oxygen were 0, 2, 3 and 4 sccm. Samples with pure CdTe absorbers are compared with samples with 50 nm CdSe evaporated on top of the CdTe layer, as mentioned above. IV and EQE measurements were done and are shown in Fig. 4.13 and Fig. 4.14.
The samples containing Selenium at the interface (green and blue line) and Oxygen in the window layer have a higher J_{SC}, FF and efficiency than the samples without Selenium (black and red line). Moreover the samples containing one CBD (black and green line) result in a better cell performance than the samples with both layers sputtered (red and blue line). The samples containing Oxygen have a local maximum at 3 sccm. On Fig. 4.13 it can be seen that the external quantum efficiency decreases with increasing amount of oxygen in the CdS. It also can be seen that the decrease is higher in the samples without Selenium at the interface to the junction.

As a further experiment instead of two times sputtered layers the whole window layer was sputtered and then treated. The results of this experiment are compared with the samples containing Selenium with the CdS layer sputtered twice and shown in Fig. 4.15. The sample with 60 nm sputtered CdS gives better cell performance than the sample with 120 nm. The V_{OC} is better in the samples where the CdS layer was deposited in two steps. FF and Efficiency are in the same range except for the sample with the 120 nm sputtered CdS layer where the efficiency is lower if the layer contains oxygen. Looking at the J_{SC}

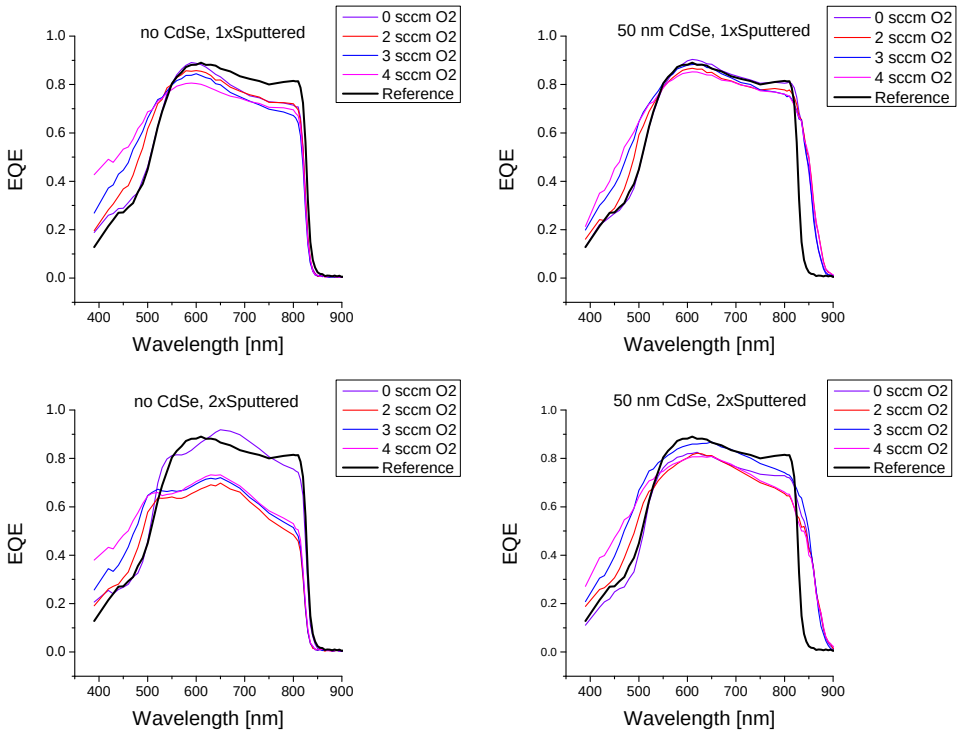

Figure 4.13: *In this Figure EQE curves of varied samples are shown. On the left hand side the samples do not contain Selenium and on the right hand side 50 nm CdSe was evaporated with the two-step evaporation method. In the samples measured in the top line the first layer of 60 nm CdS was done with CBD and the second 60 nm were sputtered with varying amounts of oxygen. For the samples shown in the bottom line twice 60 nm CdS with different amounts of oxygen were sputtered with a $CdCl_2$ treatment in between.*

in can be seen that the sample with one sputtered layer of 60 nm gives the highest values up to 3 sccm followed by the sample with one layer done by CBD. The sample with the 120 nm sputtered layer loses J_{SC} if it contains oxygen. The local maximum at 3 sccm is also visible in this experiment for the sample with the 60 nm sputtered CdS layer but not for the sample with 120 nm sputtered CdS.

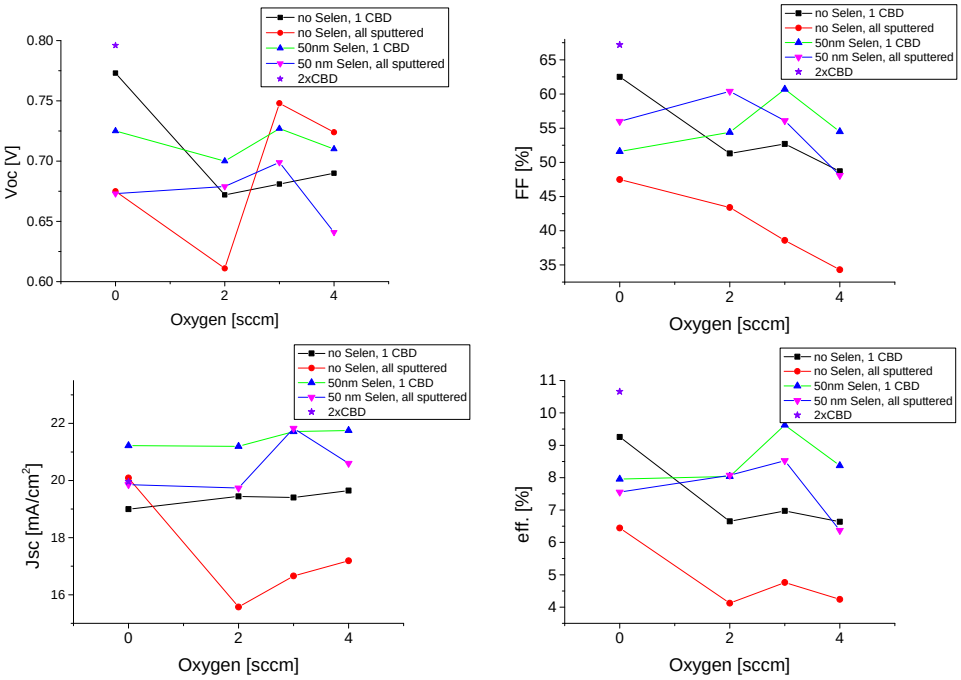

Figure 4.14: *In this Figure the samples with CdS:O are compared. The black and the red curve are the samples without Selenium. The other two contain Selenium. The violet star is the reference sample without Selenium and the standard CBD. There is a local maximum at 3 sccm for the samples containing oxygen. The samples containing both Selenium and Oxygen give the best cell performance.*

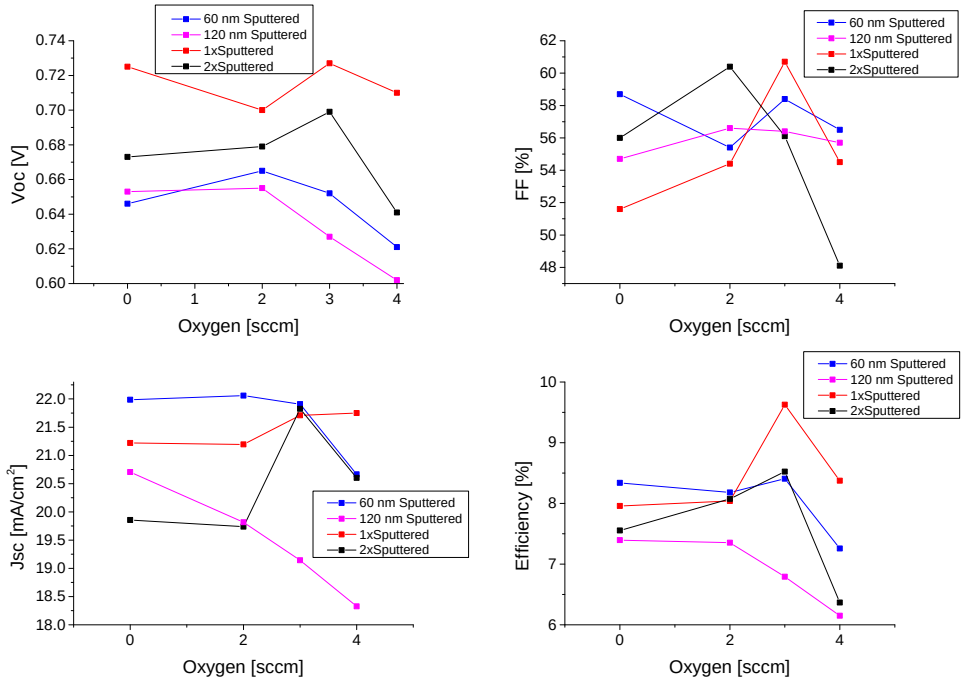

Figure 4.15: *All the samples containing Selenium with different CdS:O deposition methods are compared in this Figure. The sample with the best cell performance is the one containing 1 CBD. The local maximum at 3 sccm is also visible for the sample with 60 nm sputtered CdS.*

4.2 Discussion

In the first part the deposition and the properties of the $CdTe_{1-x}Se_x$ alloy will be analyzed. In the second part the incorporation of Selenium at the interfaces to the back contact and to the p-n junction will be discussed. At the end the influence of CdSe on the CdS and CdS:O window layer will be discussed.

The results of the ICP-OES measurements show that the measured values for the Selenium concentration are close to the expected value. This shows that the used setup for the rate control works. The inhomogeneity of Selenium of 2 % over the sample is due to the shape and position of the CdSe source (see Figure 3.1).

The band gap of the $CdTe_{1-x}Se_x$ alloy can be shifted downwards to 1.40 $\pm$ 0.02 eV at x around 0.38. This agrees with the value from literature of 1.37 $\pm$ 0.08 eV at x = 0.4 [3]. The linear parts of the Tauc plots show that the absorbance is influenced at Selenium amounts higher than 20 %. This can be because of mixed phases of the compounds which lead to different band gaps through the material. The analysis of the x-ray diffractograms shows that a mix of the zinc blende structure of CdTe and the wurzite structure of CdSe show up only after x = 0.4. They also show a peak broadening with higher amount of Selenium. Since our CdSe source in the evaporation chamber leads to an inhomogeneous distribution of Selenium in the sample (see Section 3.2.1) this could be a reason for the peak broadening. As described above the grain size decreases with increasing amount of Selenium which also lead to peak broadening as mentioned in Section 3.4.2. Since the relative intensity of the (111) peak decreases with increasing Selenium there is a change in the crystalline structure of the absorber in addition to the decreasing lattice parameter. The preferred (111) direction in pure CdTe is less pronounced in the $CdTe_{1-x}Se_x$ alloy.
A possibility to improve the cell performance is to increase the solubility of the dopant in the absorber. The results from the Hall measurements do not show an enhanced Cu solubility with incorporation of Selenium with the amounts of Cu used in this thesis. It decreases and the resistivity increases. Looking at the charge carrier density it can be seen that it increases at low amounts of Copper. It is possible that there is a charge carrier density peak at lower amounts, which was not investigated in this thesis and that the self compensation of Copper starts at lower amounts than in pure CdTe. The smaller grains are a possible reason for the increasing resistivity with increasing amount of Selenium. The fact that the resistivity decreases again with higher annealing temperatures agrees with this suggestion. Another reason for the higher resistivity is the lower amount of free charge carriers in the samples which also partly compensate the Fermi level pinning.

Incorporation of Selenium at the back and the front contact lowers the V_{OC} and FF as well as the efficiency. The J_{SC} is enhanced in both cases at low amounts. Looking at the theory the decreased band gap with Selenium is a reason for these effects. The decreased J_{SC} at higher amounts at the interface to the junction could be due to the increased resistance measured with Hall and TLM. Another explanation for the lower current could be the decrease of the amount of holes at the interface. This weakens the electric field over the junction. The strong decrease of the V_{OC} at the back contact could also be due to the lower dopability of the material. A reduction of the acceptor rate at this interface could broaden the Schottky barrier and therefor increase the recombination at the interface to the back contact.
As expected from literature the interface passivation to the CdS layer can be enhanced with incorporation of Selenium due to the reduction of the lattice parameter of absorber. This can be seen by the higher J_{SC} for samples containing low amounts of Se in Figures 4.10 to 4.12. The $CdCl_2$ treatment of the CdS layer is still necessary since the cell performance is enhanced with this treatment. The loss in the V_{OC} is too large otherwise. This is probably because Sulfur diffused into the CdTe layer helps to passivate grain boundaries and therefore reduces recombination.

Due to the enhanced interface a reduction of the CdS layer was possible. But the values of the IV parameters do not reach the values of the reference cell which is produced without CdSe and 2x18 minutes CBD for CdS. The main limiting parameter is the V_{OC} which decreases with CdSe at the interface. The optimal CdSe amount-deposition time crossing point has not been found in this work.
Another experiment to increase the J_{SC}, which was done in this work, was sputtered CdS:O. Since the possibility of depositing sputtered CdS is new at Empa the used sputtering parameters are not optimized. The sputtered CdS layer has not yet the same quality as the one done with CBD. But it is shown clearly, especially in the quantum efficiency curves in Fig. 4.13, that Se at the interface enhances the passivation to the sputtered and oxygenated window layer. The results also show that an oxygen flow of 3 sccm is a good starting point for the optimization. In Fig. 4.15 the sample with a mixture of CDB and sputtering (red) shows the best values but the 60 nm thick sputtered layer shows similar or already higher values of J_{SC}, FF and efficiency for the lower amounts of oxygen up to 3 sccm. Therefore with some optimization work also of the different annealings, this is a promising part for higher efficiencies for CdTe solar cells in substrate configuration.

4.3 Results of measurements in superstrate configuration

In this section the results of the new approach of the p-i-n junction are shown and discussed. Three runs were done for this thesis.
In the first run the thickness of the absorber layer with two different p-type layers (Spiro-OMeTad and PTAA) was investigated. In the second run the thickness of the p-type layer was increased and the results are compared with the best cells from the first run. In a third run PTAA was used as a p-type layer and the annealing of the absorber was varied.

4.3.1 Layer thickness

The first run was done to get a first impression of the needed absorber thickness. The samples were prepared as explained in Section 3.2.2 with 500 nm and 1 µm absorber thickness. The spin coating parameters for the p-type layer were the ones of variation A shown in Table 3.1. The results of the IV measurements are shown in Fig. 4.16. The current density of the samples with 500 nm intrinsic layer and Spiro-OMeTad as a p-type layer was too low to measure with the EQE curve and therefore it could not be corrected from the current measured with the IV setup which was not temperature controlled. It can be seen that except for the V_{OC} the values of the IV parameters are higher for a thicker absorber layer. Additionally it can be seen that the samples with PTAA as a p-type layer give a higher J_{SC} and efficiency.

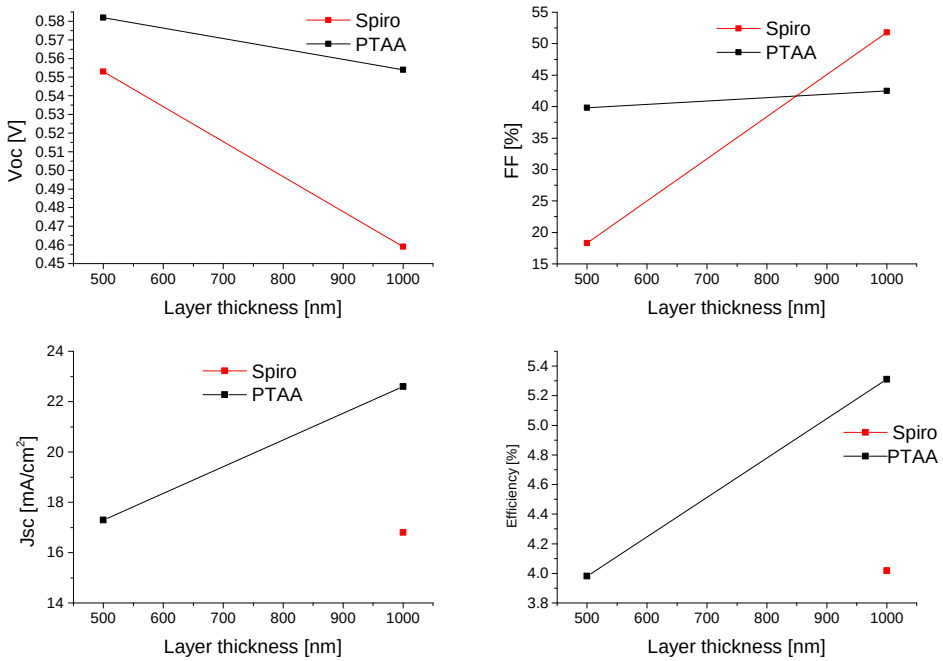

Figure 4.16: *Samples with an intrinsic layer thickness of 500 nm and 1 µm are measured. It is shown that, except for the V_{OC}, all values are higher with a thicker layer.*

4.3.2 SEM

To analyze the different layers and especially the p-type layer some SEM pictures were done from the same samples used for the investigation of the absorber thickness above. Two of them are shown on Fig. 4.17. The samples are identical up to the p-type layer (green). The $CdTe_{1-x}Se_x$ absorber (blue) has a thickness of 1 µm and x = 0.20. The 200 nm CdS layer is not visible and the absorber is directly on top of the TCO (yellow). On the left hand side the green layer is PTAA and on the right hand side it is Spiro-OMeTad . Below the TCO in the right sample the glass substrate is visible.

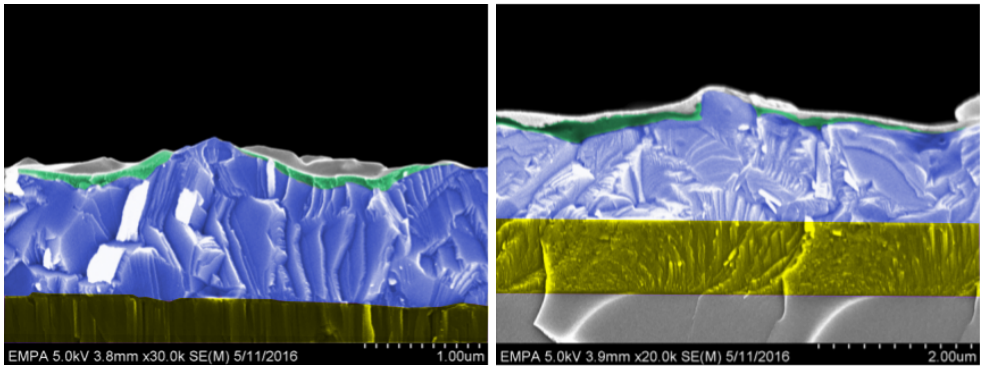

Figure 4.17: *On the left hand side a SEM picture of a p-i-n junction cell with PTAA as a p-type layer (green) is shown. The not fully covered 1 µm thick absorber (blue) is directly on top of the TCO (yellow) and the CdS layer is not visible. On the right hand side the same situation is shown with Spiro-OMeTad as a p-type layer. On top of the Spiro-OMeTad layer (green) the gold contact is visible.*

4.3.3 Thickness variations of the p-type layer

To increase the thickness of the p-type layer in a second run four different spin coating parameters were tried as shown in Table 3.1. The thickness of the layer increases from variation A to D. The parameters of variation A were the same which are used in the first run to investigate the absorber thickness above. The $CdTe_{1-x}Se_x$ alloy has a thickness of 1 µm and x = 0.25. To investigate the parameters IV and EQE measurements were done. The graphs in Fig. 4.18 show that for PTAA variation B gives the highest IV parameters and in general the samples with PTAA are better, except in the case of the V_{OC}. For the case of Spiro-OMeTad V_{OC} and J_{SC} have the highest value with variation C but FF and efficiency have the highest value with variation B.

The best variations of this run were compared with the best variation of the first run (for details see above) with an absorber thickness of 1 µm. To make a conclusion the IV parameters are compared in Fig. 4.19. Although the thickness of the p-type layer is increased, the samples from the second run show lower values of the measured IV parameters except for the V_{OC} for the samples with Spiro-OMeTad . As shown on the fifth graph of Fig. 4.19 the samples from the first run do not have the same band gap and therefore not the same amount of Selenium. The amount x was lower in the first run than in the second run. In Fig. 4.19 it is also shown that the samples with PTAA result in a better cell performance than the samples with Spiro-OMeTad .

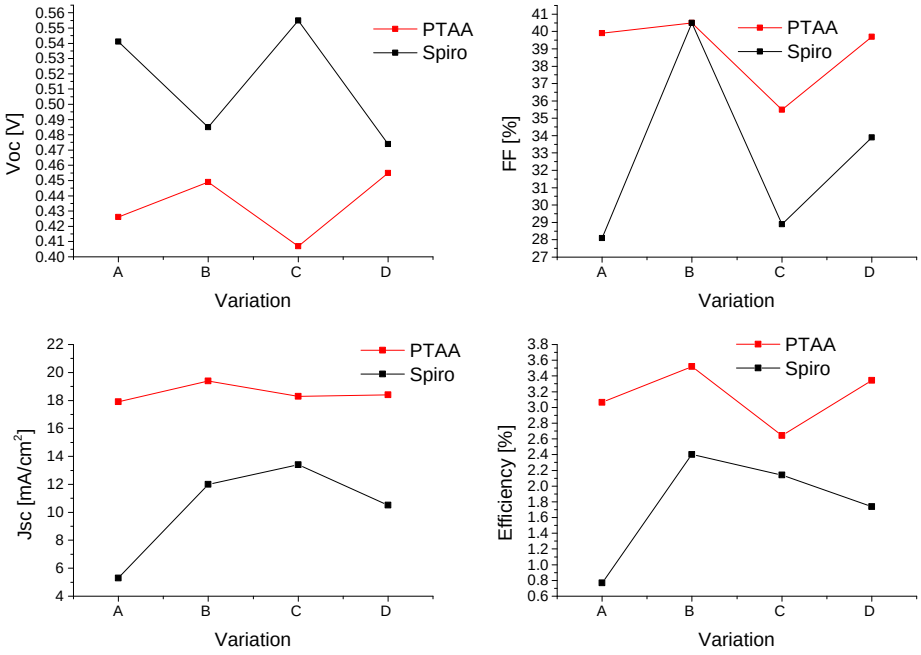

Figure 4.18: *Different p-type layer thicknesses increasing from variation A to D are investigated. The results of the IV parameters are shown in this Figure. The variations are the same for Spiro-OMeTad and PTAA and shown in the Table 3.1. For the samples with PTAA variation B gave the best results in the IV measurements. The samples with Spiro-OMeTad show a high FF with variation B but V_{OC} and J_{SC} have the highest values with variation C. The efficiency is the best with variation B.*

4.3.4 Influence of absorber and CdS annealing

Because the CdS layer vanished for annealing temperature of 460 °C annealings were conducted at lower temperatures. Additionally for two samples the CdS layer was annealed at 420 °C for 30 minutes in vacuum. Because the samples from the first run gave better results values the amount of Selenium in the alloy was x = 0.2 for two samples and for other two further decreased to x = 0.15. The IV and EQE curves were measured. The PTAA layer was done with the dynamic spin coating variation A. The IV parameters and the band gap, extracted from the EQE curves, are plotted in Figure 4.20.
During the IV measurements the samples were kept at 25 °C with the Sapphire window setup mentioned in Section 3.3.1. But because of the heat of the sun simulator the actual temperature of the cells were higher. Therefore the values of the V_{OC} and the efficiency are too low. The error on the V_{OC} is in the range of 0.03 V. The graphs show that the band gap as well as the J_{SC} drop with increasing annealing temperature. The FF increases with the temperature except for the red curve. The V_{OC} increases up to 420 °C and then it decreases. The efficiency increases from 400 °C to 410 °C. After that it further increases for the samples with a CdS annealing, and decreases for the ones without.

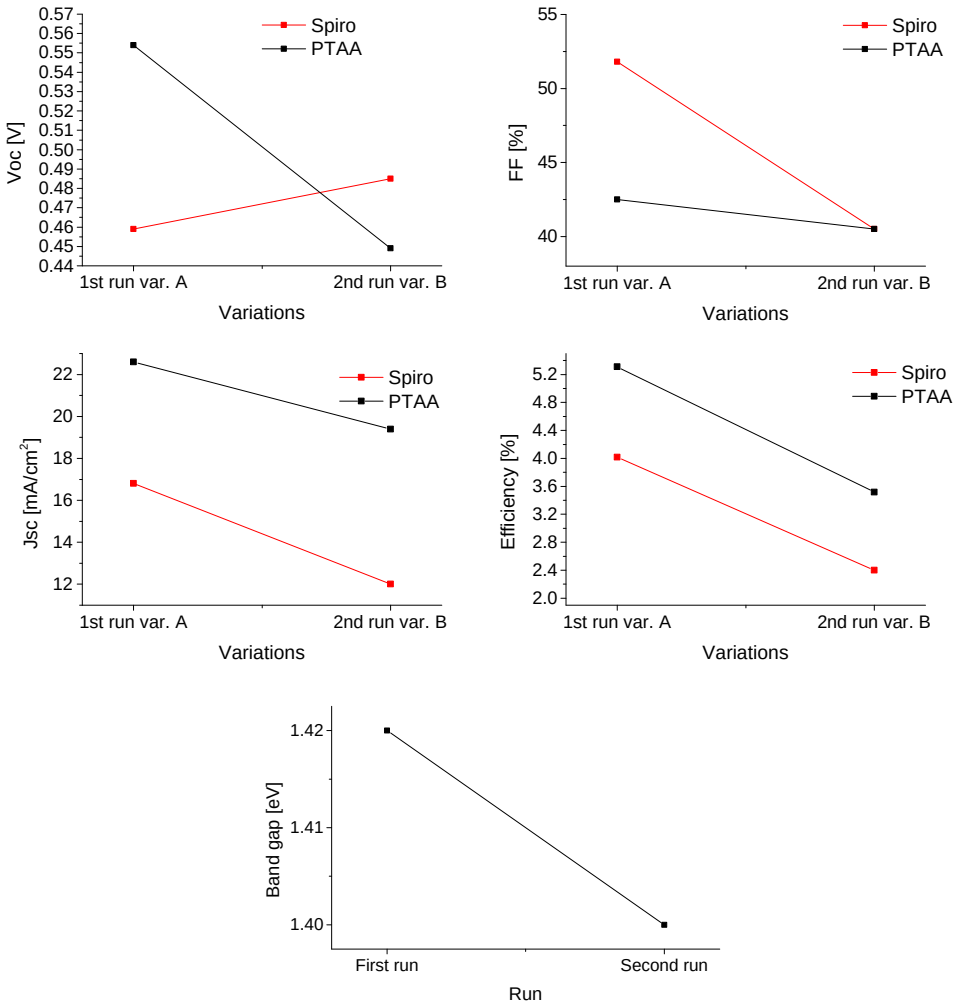

Figure 4.19: *Variation B of this second run is compared with the best sample from the first run (see above Section 4.3.1). In every case variation A in the first run gave the best results but the V_{OC} for the samples with Spiro-OMeTad increases with increasing p-layer thickness. On the fifth graph it is shown that the band gap of the samples from the first run is larger than the one of the samples from the second run.*

4.4 Discussion

In this section the results of the samples with the p-i-n junction are analyzed. The idea for this experiments is based on the Hall measurements of the alloy which show a high resistivity. This makes the alloy to an interesting candidate for an intrinsic layer.

Looking at the results of the thickness of the alloy in Section 4.3.1 the thicker layer seems to be better. The V_{OC} is higher for the thinner layer which is probably due to an enhanced recombination rate in a thicker layer. The J_{SC} is probably higher in the thicker layer due to the larger depletion region. Since the region is wider, more charge carriers are excited to the conduction band and get separated immediately and forced to the corresponding layers.
A conclusion about the amount of Selenium can not be made. The band gaps shown in Fig. 4.20 for samples with an absorber annealing at 400 °C have values higher than 1.45, which is expected for an amount of Se of 10 % or less. Therefore there is less Selenium in the samples than expected and the

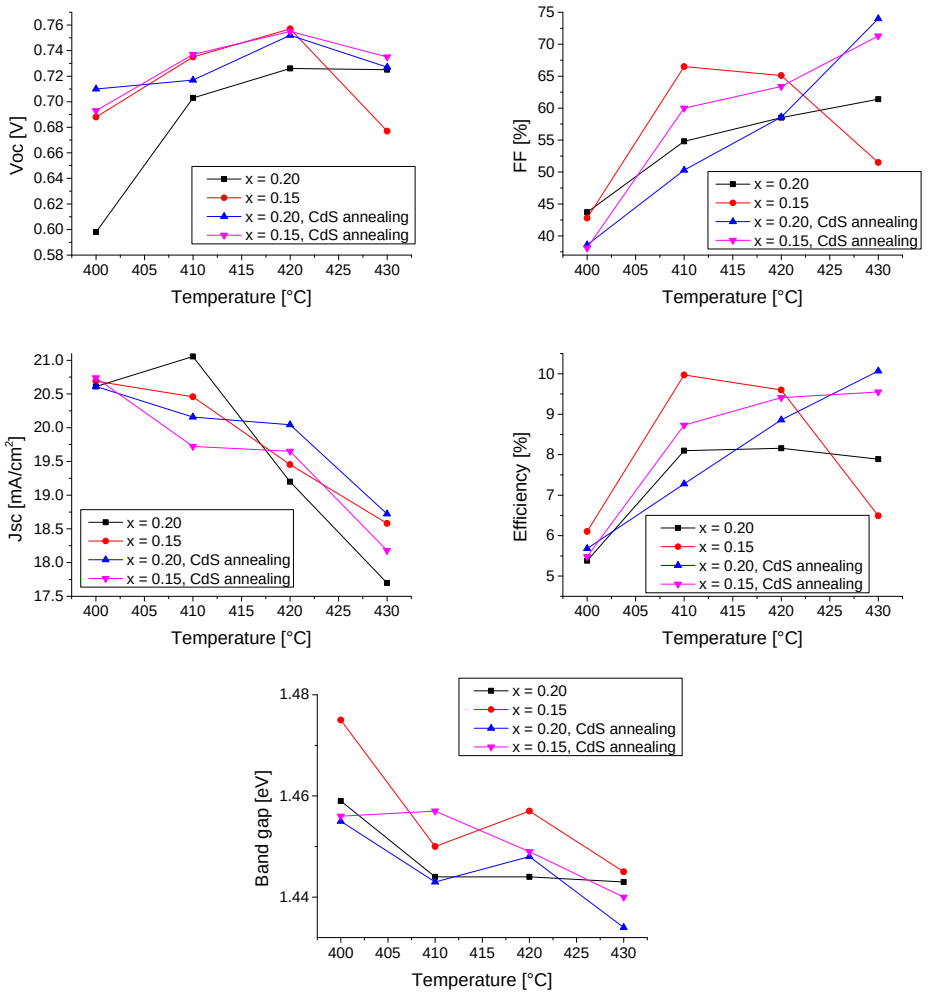

Figure 4.20: *The upper four Figures shows the results of IV measurements for samples with different absorber annealing temperatures. The band gap in the last picture is extracted from the EQE curve. The V_{OC} and the efficiency values are too low because of experimental limitations.*

experiment has to be done again. But Fig. 4.18 shows that a Selenium amount of x = 0.20 gives a higher cell performance than x = 0.25 therefore the next experiments should be with Se amount of x = 0.2 or lower.

The SEM pictures show that the absorber annealing at 460 °C was too high because the CdS layer is not visible anymore. This means that the CdS layer is alloyed with the material of the intrinsic layer. This results in a region where a lot of recombination happens, which reduces the V_{OC}. These pictures also show that the surface roughness of CdTe is too high for the used spin coating method. The p-type layer does not cover the alloy completely.This also limits the performance of the cell. Because of the strong zigzag behavior of the FF and V_{OC} visible in Fig. 4.18, it seems that the coverage problem is still not solved with the investigated variations. To analyze it properly SEM pictures have to be done again. PTAA variation B could be a good starting point because it gives the best cell performance. There are also other possibilities to overcome the problem of a high surface roughness which were discussed with the Perovskite specialists in the group. An example is to deposit, after applying the spin coated layer, the cheaper and evaporated MoO_3 to cover the whole layer. These experiments are not done yet.
That the J_{SC} for Spiro-OMeTad is lower than for PTAA is probably due to the band properties. The

valence bands of Spiro-OMeTad and CdTe are both at -5.2 eV, the one of PTAA at -5.1 eV (see Section 3.2.2). If CdTe is alloyed with CdSe the band gap decreases, mainly influencing the valence band (see Chapter 1). Therefore the valence band of the intrinsic layer lifts and a small Schottky barrier for the holes is formed. The smaller FF and the increased V_{OC} for Spiro-OMeTAD at the smaller band gap in Fig. 4.18 agree with this argumentation. Since this barrier is still small enough to overcome for some holes it introduces a resistance which could be responsible for the higher V_{OC} in some samples with Spiro-OMeTad.
The V_{OC} drop for PTAA in Figure 4.19 agrees with the theory of a lower voltage at a smaller band gap. The decrease of the J_{SC} is probably due to the high resistivity in the alloyed material as in the case of the cells in substrate configuration.

The results in Section 4.3.4 show an interesting effect. Despite the decreasing band gap the J_{SC} decreases and the V_{OC} increases which is the opposite what is expected from theory (see Section 2.3.1). The decrease of the band gap and the V_{OC} at 430 °C can be explained with the intermixing of CdS with CdTe. Due to the band gap bowing shown in 1 this intermixing leads to a decrease of the band gap. It is known that the $CdTe_{1-x}CdS_x$ alloy leads to enhanced recombination. The decrease of the current can be caused by a weaker field due to the reduced CdS layer. The enhanced V_{OC} can be due to an increased resistivity in the CdTe/CdS intermixed part before the intermixing is too high and causes too much recombination as assumed at 430 °C.
The strong decrease of the red curve visible in Figure 4.20 at 430 °C in FF and V_{OC} and therefore also in the efficiency is probably due to the used dynamic spin coating which does not cover the alloy completely (see Section 4.3.2). It is possible that for this sample the coverage is worse. Another explanation is the missing CdS annealing. It is known that it lowers the amount of intermixing of CdS and CdTe. Looking at the values it can be seen that the V_{OC} is increased compared to the first experiments and reaches almost the V_{OC} values of the standard substrate CdTe solar cells. It has to be considered that the measured V_{OC} values are up to 0.03 V lower than the actual values due to the temperature during the IV measurements. The J_{SC} and the FF are already in the order of the standard CdTe cells. The efficiency already reaches 9 to 10 %. Here again it has to be considered that the actual value is about 0.3 % higher.

5

Conclusion and Outlook

An efficiency enhancement of the CdTe solar cell in substrate configuration by alloying CdTe with CdSe was not observed in this work. One reason is the decreased charge carrier concentration. Two possibilities for further experiments are either to go to smaller Copper amounts and see if there is a charge carrier density peak at lower amounts, or change the dopant. Possible Copper replacements are Phosphorus or Arsenic. Another reason is the reduced V_{OC} due to enhanced recombination. To minimize the loss in the V_{OC} optimization experiments have to be done.
Although the cell efficiency could not be increased in this work, the incorporation of low amounts of Selenium in CdTe solar cells seems to be a promising approach, especially incorporated at the interface to the oxygenated CdS window layer. The experiments done in this thesis show that the current density can be enhanced with this method.

The p-i-n junction cells investigated in this thesis showed already an efficiency over 10 % with V_{OC}, J_{SC} and FF in the same range as the standard CdTe cells. Since this is a very new approach all the parameters and layers are not optimized. But since already the first experiments showed this promising cell performance and there are a lot improvement opportunities, this is a very interesting concept. The focus at the beginning should be to find a proper p-type layer coverage. There are several ideas as for example depositing on top of the chosen p-type layer the cheaper and evaporated MoO_3 to cover the whole layer. To enhance the junction quality the doping of the p-layer can be varied. Especially an increase in the J_{SC} can be achieved by varying the thickness of the CdS layer. Another idea is to replace CdS with oxygenated CdS or TiO_2.

A

Appendix

A.1 Glossary

Table A.1: *The most used abbreviations are listened and explained in this table.*

Abbreviation	Meaning
HVE	High vacuum evaporation
CBD	Chemical bath deposition
SEM	Scanning electron microscope
EDX	Energy dispersive x-ray spectroscope
ICP-OES	Inductively coupled plasma optical emission spectroscopy
XRD	X-ray diffraction
EQE	External quantum efficiency
IV curve	Current Voltage curve
V_{OC}	Open circuit voltage
J_{SC}	Short circuit current density
FF	Fill factor
sccm	Standard cubic centimeters per minute
rpm	Rotations per minute
Spiro-OMeTAD	2,2',7,7'-Tetrakis-(N,N'-di-4-methoxyphenylamino)-9,9'-spirobifluorene
PTAA	Poly[bis(4-phenyl)(2,4,6-trimethylphenyl)amine]

A.2 PTAA and Spiro-OMeTAD

Spiro-OMeTAD and PTAA are organic polymers. Their whole names, which determine position, amount and atoms of the molecules are shown in Table A.1. The composition of the spin coated solutions are the following:

Spiro-OMeTAD solution: 72.3 mg Spiro-OMeTAD, 17.5 µl Li-TFSI (lithium-bis(trifluoromethanesulfonyl)imide) solution (520 mg Li-TFSI in 1 ml acetonitrile), and 28.8 µl TBP (4-tertbutylpyridine) were dissolved in 1000 µl chlorobenzene.

PTAA solution: PTAA was dissolved in Toluene (5 mg/ml) and with 1 weight-% T-4-TCNQ (2,3,5,6-Tetrafluoro-7,7,8,8-tetracyanoquinodimethane).

A.3 ICP-OES results for x = 0.2

Table A.2: *The ICP-OES results of the sample with the expected x = 0.2 are shown.*

Cd [µmol/L]	Te [µmol/L]	Se [µmol/L]	at% Cd	at% Te	at% Se
453.25	358.23	80.28	50.83	40.17	9.00
579.21	438.64	113.84	54.18	38.76	10.06
605.37	442.87	134.73	51.17	37.44	11.39

Bibliography

[1] EPFL press release: Perovskite solar cells surpass 20 % efficiency. https://documents.epfl.ch/groups/e/ep/epflmedia/www/20160609_Perovskite/PressRelease_Graetzel_EN.pdf, retrieved on 09/06/2016.

[2] S. R. A. and K. P. C. *Growth and characterisation of semiconductors*. Adam Hilger, 1991.

[3] F. Z. Amir, K. Clark, E. Maldonado, W. P. Kirk, J. C. Jiang, J. W. Ager, K. M. Yu, and W. Walukiewicz. Epitaxial growth of CdSexTe1-x thin films on Si(1 0 0) by molecular beam epitaxy using lattice mismatch graded structures. *Journal of Crystal Growth*, 310(6):1081–1087, 2008.

[4] C.-c. Chueh, C.-z. Li, and A. K. Jen. Environmental Science Recent progress and perspective in solution- processed Interfacial materials for e ffi cient and stable polymer and organometal perovskite solar cells. *Energy & Environmental Science*, 00:1–30, 2015.

[5] J. Daniel. http://physik2.uni-goettingen.de/research/2_hofs/methods/XRD, Accessed: 01/06/2016.

[6] R. G. Dhere, J. N. Duenow, C. M. Dehart, J. V. Li, D. Kuciauskas, and T. A. Gessert. Development of substrate structure CdTe photovoltaic devices with performance exceeding 10%. *Conference Record of the IEEE Photovoltaic Specialists Conference*, (August):3208–3211, 2012.

[7] C. Gretener, J. Perrenoud, L. Kranz, K. Luisa, R. Schmitt, S. Buecheler, and A. N. Tiwari. Solar Cells Utilizing Small Molecular Weight Organic Semiconductors. *Prog. Photovolt: Res. Appl.*, 15(February 2013):659–676, 2007.

[8] C. A. Gretener. *Back contact , doping and stability of CdTe thin film solar cells in substrate configuration*. PhD thesis, 2015.

[9] R. Gross and A. Marx. *Festkörperphysik*. De Gruyter, 2014.

[10] C. Honsberg and S. Bowden. http://www.pveducation.org/, Accessed: 06/05/2016.

[11] J. M. Kephart, R. Geisthardt, and W. S. Sampath. Sputtered, Oxyganeted CdS Window Layers for Higher Current in CdS/CdTe TThin Film Solar Cells. *IEEE Access*, pages 854–858, 2011.

[12] L. Kranz, C. Gretener, J. Perrenoud, R. Schmitt, F. Pianezzi, F. La Mattina, P. Blösch, E. Cheah, A. Chirilă, C. M. Fella, H. Hagendorfer, T. Jäger, S. Nishiwaki, A. R. Uhl, S. Buecheler, and A. N. Tiwari. Doping of polycrystalline CdTe for high-efficiency solar cells on flexible metal foil. *Nature Communications*, 4:2306, 2013.

[13] S. G. Kumar and K. S. R. K. Rao. Physics and chemistry of CdTe/CdS thin film heterojunction photovoltaic devices: fundamental and critical aspects. *Energy Environ. Sci.*, 7(1):45–102, 2014.

[14] H. Lund, F. Nilsen, O. Salomatova, D. Skare, and E. Riisem. http://org.ntnu.no/solarcells/pages/Chap5.php, Accessed: 20/05/2016.

[15] J. Ma and S.-H. Wei. Bowing of the defect formation energy in semiconductor alloys. *Physical Review B*, 87(24):241201, 2013.

[16] R. A. Meyers. *Encyclopedia of Sustainability Science and Technology*. Springer, 2012.

[17] S. Montanari. *Fabrication and characterization of planar Gunn diodes for Monolithic Microwave Integrated Circuits . Herstellung und Charakterisierung planarer Gunn-Dioden für monolitisch Controlled Oscillator Monolithic Microwave Integrated Circuit* . PhD thesis, 2005.

[18] A. Mukerjee and N. Thakur. *Photovoltaic systems*. PHI, 2011.

[19] Ossila. http://www.ossila.com/pages/spin-coating, Accessed: 01/06/2016.

[20] N. R. Paudel, J. D. Poplawsky, K. L. Moore, and Y. Yan. Current Enhancement of CdTe-Based Solar Cells. *IEEE Journal of Photovoltaics*, 5(5):1492–1496, 2015.

[21] J. Perrenoud, L. Kranz, C. Gretener, F. Pianezzi, S. Nishiwaki, S. Buecheler, and a. N. Tiwari. A comprehensive picture of Cu doping in CdTe solar cells. *Journal of Applied Physics*, 114(17):174505, 2013.

[22] M. K. Rabadanov, I. a. Verin, Y. M. Ivanov, and V. I. Simonov. Refinement of the atomic structure of CdTe single crystals. *Crystallography Reports*, 46(4):636–641, 2001.

[23] J. H. Rhee, C.-C. Chung, and E. W.-G. Diau. A perspective of mesoscopic solar cells based on metal chalcogenide quantum dots and organometal-halide perovskites. *NPG Asia Mater*, 5(10):e68, 2013.

[24] M. Sardela. https://mrl.illinois.edu/sites/default/files/pdfs/Workshop08_X-ray_Handouts.pdf, Accessed: 06/06/2016.

[25] W. Shockley and H. J. Queisser. Detailed balance limit of efficiency of p-n junction solar cells. *Journal of Applied Physics*, 32(3):510–519, 1961.

[26] N. Tit, I. M. Obaidat, and H. Alawadhi. Origins of bandgap bowing in compound-semiconductor common-cation ternary alloys. *Journal of physics: condensed matter*, 21(7):075802, 2009.

[27] S.-H. Wei, S. B. Zhang, and A. Zunger. First-principles calculation of band offsets, optical bowings, and defects in CdS, CdSe, CdTe, and their alloys. *Journal of Applied Physics*, 87(2000):1304, 2000.

[28] C. A. Wolden, A. Abbas, J. Li, D. R. Diercks, D. M. Meysing, T. R. Ohno, J. D. Beach, T. M. Barnes, and J. M. Walls. The roles of ZnTe buffer layers on CdTe solar cell performance. *Solar Energy Materials and Solar Cells*, 147:203–210, 2016.

[29] Y.-N. Xu and W. Ching. Electronic, optical, and structural properties of some wurtzite crystals. *Physical Review B*, 48(7):4335–4351, 1993.